

Vibrational Spectra of Materials and Molecules from Partially-Adiabatic Elevated-Temperature Centroid Molecular Dynamics

Jorge Castro,¹ George Trenins,¹ Venkat Kapil,^{2,3} and Mariana Rossi¹

¹Max Planck Institute for the Structure and Dynamics of Matter, Hamburg, Germany

²Department of Physics and Astronomy, University College London, 7-19 Gordon St, London WC1H 0AH, UK

³Thomas Young Centre and London Centre for Nanotechnology, 9 Gordon St, London WC1H 0AH

(*Electronic mail: mariana.rossi@mpsd.mpg.de)

(Dated: 25 August 2025)

Centroid molecular dynamics (CMD) incorporates nuclear quantum statistics into the calculation of vibrational spectra. However, when performed in Cartesian coordinates, CMD shows serious unphysical artifacts in certain vibrational bands, known as the curvature problem. Recent work showed that CMD spectra can be freed from the curvature problem by evolving the ring-polymer centroid on a potential of mean force (PMF) calculated at an elevated temperature (T_e -CMD). Here we present a partially-adiabatic implementation of T_e -CMD (PA- T_e -CMD), which eliminates the need for precomputed PMFs and instead yields the centroid force *on-the-fly*. We introduce a two-temperature path-integral Langevin thermostat to achieve a temperature separation between centroid and internal modes of the ring-polymer. Because it is paramount that the elevated temperature be chosen as low as possible for a given physical temperature in this formulation, we present a general scheme for its determination. We benchmark PA- T_e -CMD against exact vibrational spectra for the isolated water monomer and discuss its performance for challenging anharmonic systems: the carbonic acid fluoride molecule (CAF) and the methylammonium lead iodide perovskite (MAPI). We conclude that PA- T_e -CMD mitigates the curvature problem and eliminates the steep increase in computational cost with decreasing temperature of conventional path-integral methods. We observe some energy leakage from the hot internal modes to high-frequency centroid modes at low physical temperatures. Nevertheless, compared to other imaginary path-integral approximate methods, the PA- T_e -CMD spectra show more accurate lineshapes. While a fully adiabatic setup based on a coarse-grained centroid PMF is still preferable when a good pre-trained PMF can be easily obtained, PA- T_e -CMD presents a low-barrier single-shot setup for any system.

I. INTRODUCTION

Nuclear quantum effects can be critical in vibrational spectroscopy, where they modulate the position, shape, and intensity of spectral features. Striking examples include redshifts and line-shape variations observed in hydrogen-bonded systems^{1–6}, at aqueous interfaces^{7–9}, in molecular crystals and in confined environments^{10–12}. Despite the theoretical foundation that quantum mechanics provides, solving the many-body time-dependent Schrödinger equation (TDSE) is computationally prohibitive for systems with more than a few tens of atoms. As a result, several approximate quantum many-body methods have been developed since the late 1990s, achieving varying degrees of success in bridging the gap between classical and quantum descriptions^{13–17}.

Computational methods for vibrational spectroscopy that go beyond the standard harmonic treatment of nuclear motion broadly fall into two categories: methods that target a solution of the TDSE with varying levels of approximations and methods that try to approach quantum mechanics from modifications to classical dynamics. Techniques in the first category can provide near-exact quantum results. While these methods are well suited for small molecules or systems in which only a limited subset of degrees of freedom is relevant, their computational cost limits their applicability to larger and more complex systems. Prominent examples include the multi-configurational time-dependent Hartree (MCTDH) method¹⁸, quantum-classical path integrals¹⁹, hierarchical equations of motion (HEOM)²⁰, and vibrational self-

consistent field (VSCF) approaches^{21–24}.

In contrast, techniques in the second category are computationally efficient and well-suited for simulating all degrees of freedom in large systems. For example, simply using classical molecular dynamics to approximate vibrational motion is straightforward, but inherently ignores any nuclear quantum effects (NQE). Approximations based on imaginary-time path integral molecular dynamics (PIMD) provide an exact quantum statistical framework where time-independent observables can be sampled with classical trajectories on an extended phase-space spanned by a ring-polymer representation of the system^{25–27}. Extending this framework to simulate time-dependent properties, such as vibrational spectra, without resorting to computationally prohibitive real-time path integrals^{28–30}, necessarily relies on (uncontrolled) approximations for the dynamics. Among the most widely used approaches are centroid molecular dynamics (CMD)^{31,32} and (thermostatted) ring-polymer molecular dynamics [(T)RPMD]^{33–37}.

These methods approximate thermal quantum time-correlation functions in different ways. CMD propagates dynamics on the centroid potential of mean force (PMF) generated by thermal fluctuations of the ring polymer internal modes. In contrast, (T)RPMD considers the classical dynamics of the ring-polymer in its full extended phase space. TRPMD is often favored for its computational efficiency, whereas CMD provides a more direct statistical mechanical interpretation through the centroid probability density. Although originally introduced heuristically, these meth-

ods were shown to be different approximations to Matsubara dynamics^{38,39}, thus representing different ways to join quantum statistics with classical dynamics. Over the past decade, extensive work has demonstrated both the strengths and limitations of CMD and TRPMD for vibrational spectroscopy in a wide variety of systems spanning molecules, liquids and solids^{1-6,8,10,11,40-59}.

A limitation of particular relevance to this work regards the CMD method. The well-documented “curvature problem”^{60,61} is an artifact that arises when CMD is performed in Cartesian coordinates⁵⁹. For systems where curvilinear vibrational motion is possible, coupling between stretching and angular modes of the ring-polymer can cause the centroid to drift outside the ring-polymer hull as the temperature is lowered. The result is an unphysical and pronounced red-shift and broadening of vibrational peaks^{36,59-61}. In addition, the curvature problem can also distort vibrational intensities by altering the distribution of spectral weight. An illustration of this effect is presented in Section S1 of the SI.

Techniques such as quasi-centroid molecular dynamics (QCMD)⁵⁹ and fast-QCMD⁶² avoid the curvature problem by evolving the system on the free energy surface of a carefully chosen curvilinear function of ring-polymer bead positions. However, extending both QCMD and fast-QCMD to general systems requires a universal free-energy fitting procedure and careful selection of curvilinear coordinates⁶³ to ensure accurate spectra and comprehensive configurational sampling.

An alternative method that mitigates the curvature problem is the “elevated-temperature” CMD method⁶⁴ (T_e -CMD). In this approach, the centroid potential of mean force (PMF) is computed at an elevated temperature T_e , where the curvature problem is negligible, while the system evolves at the physical temperature. In the original implementation⁶⁴, a path-integral coarse-graining force-matching protocol was used in order to train a machine-learning force-field for the centroid PMF based on a reference PIMD simulation. This approach is referred to as PIGS. To attenuate the curvature problem, the reference PIMD simulations are performed at a high temperature T_e . After the PMF is trained, the evaluation of a T_e -CMD vibrational spectrum only requires running classical molecular dynamics at any desired physical temperature and constructing the desired correlation function. The resulting spectra are free of the curvature problem and still capture the relevant quantum statistical effects related to zero-point energy motion. T_e -PIGS was shown to be successful for molecular and condensed-phase systems, even for cryogenic physical temperatures^{7,64,65}.

Performing a T_e -PIGS simulation inherently involves two steps: training the PMF and subsequently running the simulation. Because the PMF is typically constructed by combining a baseline machine-learned (ML) interatomic potential with an additional ML model that upgrades it to the PMF, it also opens the possibility of compounded errors in the forces. However, just as in standard CMD, it should also be possible to calculate vibrational spectra within the T_e -CMD framework with an on-the-fly partially adiabatic (PA) protocol. In this work, we introduce precisely this approach. In partially-adiabatic T_e -CMD (PA- T_e -CMD) the centroid PMF is com-

puted during the simulation, eliminating the need for precomputed models. The method combines the mass rescaling strategy of PA-CMD⁶⁶, which assigns lighter fictitious masses to the internal ring-polymer modes to accelerate their dynamics, with the elevated-temperature *ansatz* enforced through a two-temperature path-integral Langevin thermostat⁶⁷. This setup efficiently samples the high-temperature PMF while keeping the centroid at the physical temperature. As a result, PA- T_e -CMD offers a single-shot alternative to T_e -PIGS, improving transferability and ease of use while preserving the core features of the elevated-temperature approach. The most notable compromise is the necessity of using smaller time-steps in the simulation.

In the following, we describe the PA- T_e -CMD method in detail, provide guidelines for choosing T_e for different systems, and benchmark its performance against exact spectra, where available, and against other path-integral-based methods such as CMD, TRPMD, and T_e -PIGS. For an isolated water monomer, PA- T_e -CMD closely reproduces the results of T_e -PIGS and the exact vibrational density of states and infrared spectra. For methylammonium lead iodide (MAPI), accurate spectra for its tetragonal and orthorhombic phases are obtained from PA- T_e -CMD and compare well with T_e -PIGS, showing that the latter performs well even when the lower temperature simulations are run with a PMF trained on the high-temperature cubic phase. Finally, for the carbonic acid fluoride molecule $[\text{H}_2\text{CO}_3\text{F}]^-$ (CAF) we find it more difficult to obtain accurate centroid PMFs for use with T_e -PIGS due to the weakly-bound nature of the complex. In this case, PA- T_e -CMD offers a good alternative for obtaining accurate vibrational fingerprints. Overall, we observe that it is more challenging to maintain the temperature separation between centroid and internal modes of the ring polymer in PA- T_e -CMD when the physical temperature is substantially low. Nevertheless, PA- T_e -CMD proves to be simple to set up for any system and to provide a reliable route to obtain vibrational spectra of condensed-phase systems and molecules, in regimes where nuclear quantum coherences are naturally suppressed by temperature and many-body interactions.

II. METHODS

A. Centroid Molecular Dynamics

Centroid molecular dynamics (CMD) provides an approximation to quantum Kubo-transformed time-correlation functions^{31,32,66,68} of the form

$$K_{AB}(t, \beta) = \frac{1}{\beta Z} \int_0^\beta d\lambda \text{tr}[e^{-(\beta-\lambda)\hat{H}} \hat{A} e^{-\lambda\hat{H}} \hat{B}(t)], \quad (1)$$

where $Z = \text{tr}[e^{-\beta\hat{H}}]$ is the canonical quantum partition function, $\beta = 1/k_B T$ is the inverse temperature, $\hat{B}(t) = e^{+i\hat{H}t/\hbar} \hat{B} e^{-i\hat{H}t/\hbar}$, \hat{H} is the Hamiltonian of the system and t is the physical time.

Like other PIMD-based methods, CMD can be obtained from the dynamics of a fictitious ring-polymer Hamiltonian.

For a one-dimensional system with P replicas, this Hamiltonian can be written in terms of the free ring-polymer normal modes as

$$\mathcal{H}_P = \sum_{k=0}^{P-1} \left(\frac{\tilde{\mathbf{p}}_{(k)}^2}{2m} + \frac{1}{2} m \omega_k^2 \tilde{\mathbf{q}}_{(k)}^2 \right) + \tilde{V}_P(\tilde{\mathbf{q}}), \quad (2)$$

where $\tilde{\mathbf{q}}$ and $\tilde{\mathbf{p}}$ are the positions and momenta, respectively, transformed into the free ring-polymer normal-mode basis. For the transformation, we employ the same normalization convention as Ref. 69, such that the zeroth ring-polymer normal mode is the centroid $\mathbf{q}_c \equiv \tilde{\mathbf{q}}_{(0)}$. Here, $\omega_k = 2P/(\beta\hbar) \sin(k\pi/P)$ are the frequencies of the normal modes, and $\tilde{V}_P(\tilde{\mathbf{q}})$ is the average of the physical potential over the ring-polymer beads. For multidimensional systems, this expression generalizes straightforwardly by summing over all Cartesian degrees of freedom.

For operators \hat{A} and \hat{B} that are either functions of the position operator or proportional to the momentum operator, the CMD approximation to the KTCF can then be written as

$$K_{AB}(t, \beta) \approx \frac{1}{Z} \int d\mathbf{q}_c \int d\mathbf{p}_c \times A[\mathbf{q}_c(0)] B[\mathbf{q}_c(t)] e^{-\beta \left(\frac{\mathbf{p}_c^2}{2m} + \bar{U}(\mathbf{q}_c, \beta) \right)}, \quad (3)$$

where $\bar{U}(\mathbf{q}_c, \beta)$ is the PMF for the centroid, computed by averaging over the non-centroid normal modes of the ring polymer

$$\bar{U}(\mathbf{q}_c) = -\frac{1}{\beta} \ln \left[\lim_{P \rightarrow \infty} \langle \delta(\tilde{\mathbf{q}}_{(0)} - \mathbf{q}_c) \rangle \right]. \quad (4)$$

The thermodynamic average $\langle \cdot \rangle$ is calculated with the ring-polymer Hamiltonian of Eq. (2). As an example, to obtain the vibrational density of states, Eq. (3) needs to be evaluated with A and B set to the centroid velocity.

The centroid dynamics follow simple classical equations of motion,

$$\begin{aligned} \frac{d\mathbf{q}_c}{dt} &= \frac{\mathbf{p}_c}{m}, \\ \frac{d\mathbf{p}_c}{dt} &= -\frac{\partial \bar{U}(\mathbf{q}_c)}{\partial \mathbf{q}_c}. \end{aligned} \quad (5)$$

The centroid PMF can either be precomputed (e.g., on a grid or with a fitted functional form) or computed on-the-fly. The latter is achieved by imposing an adiabatic separation between the dynamics of the centroid and non-centroid modes. In partially adiabatic CMD (PA-CMD)⁶⁶, the fictitious masses of the non-centroid normal modes are rescaled to a fraction of the value of the lightest chemical species in the system, while keeping the mass of the centroids equal to the physical masses. The PA-CMD Hamiltonian can be written as

$$\mathcal{H}_P = \sum_{k=0}^{P-1} \left(\frac{\tilde{\mathbf{p}}_{(k)}^2}{2m_k} + \frac{1}{2} m_k \Omega^2 \tilde{\mathbf{q}}_{(k)}^2 \right) + \tilde{V}_P(\tilde{\mathbf{q}}), \quad (6)$$

where Ω is the frequency of adiabatic separation, $m_k = m/\sigma_k^2$, and σ_k is the adiabatic scaling parameter,

$$\sigma_k = \begin{cases} 1 & \text{for } k=0, \\ \Omega/\omega_k & \text{otherwise.} \end{cases} \quad (7)$$

The scaling is defined such that $m_k \Omega^2 = m \omega_k^2$, so the ring-polymer quantum statistics are not altered by this renormalization.

The choice of Ω is critical to the accuracy and efficiency of the CMD. By setting this frequency to a value much larger than any physical vibration in the system, one enables dynamical sampling of $\bar{U}(\mathbf{q}_c)$ as the centroid moves on a slower timescale. However, a larger Ω increases the highest dynamical frequency in the system, requiring smaller time steps for accurate integration of the equations of motion. In practice, Ω is selected as a compromise between convergence and computational efficiency, balancing accurate PMF sampling with a reasonably large timestep. Efficient sampling of the PMF requires that strongly coupled thermostats are applied to the non-centroid modes, and we note that the choice of thermostat and its parameters also affects the choice of Ω , as discussed in Ref. 41.

B. The Elevated Temperature Ansatz

It is well documented that at low temperatures, a vibrational spectrum calculated from the CMD correlation function in Eq. (3) presents the so-called curvature problem⁶¹. Ultimately, this problem stems from the use of Cartesian coordinates to calculate the PMF⁵⁹, and different techniques have been proposed to mitigate it. In particular, Musil *et al.*⁶⁴ introduced the elevated temperature (T_e) *ansatz* that effectively mitigates the curvature problem because at T_e a curvilinear centroid is well approximated by its Cartesian counterpart.

This approach exploits the fact that in a system in the vibrational ground state ($\hbar\omega \gg k_B T$), the exact quantum time-correlation function is temperature-independent. Hence, a low-temperature KTCF can be obtained by simulating the system at an elevated temperature T_e that is high enough to suppress the curvature problem but low enough for the system to remain in the vibrational ground state. The Fourier transform of the KTCF satisfies⁶⁴

$$K_{AB}(\omega, \beta; \beta_e) = \frac{\beta_e}{\beta} K_{AB}^e(\omega, \beta_e), \quad (8)$$

where $\beta_e = 1/(k_B T_e)$. The term K_{AB} is proposed to be approximated as

$$K_{AB}(\omega, \beta; \beta_e) \approx \frac{1}{Z} \mathfrak{F} \left[\int d\mathbf{q}_c d\mathbf{p}_c A[\mathbf{q}_c(0)] B[\mathbf{q}_c(t)] \times \exp \left(-\beta \left[\frac{\mathbf{p}_c^2}{2m} + \bar{U}(\mathbf{q}_c, \beta_e) \right] \right) \right], \quad (9)$$

which is exact in the harmonic and in the classical limit.

Thus, the elevated temperature *ansatz* requires the computation of the centroid PMF at T_e and the evaluation of the centroid dynamics at the target temperature T . This has proven to

be an excellent approximation for vibrational spectra^{9,64,70–72} and for the efficient evaluation of static properties.⁷³ We call this approximation T_e -CMD in the following.

C. A Practical Recipe for Choosing the Elevated Temperature

The elevated temperature for T_e -CMD should be chosen with care. It must be high enough to avoid the curvature problem, but not so high that it breaks the approximation in Eq. (9). In Ref. 64, it was proposed to determine T_e by performing PIMD simulations at a range of temperatures and selecting the lowest temperature at which the mode of the radial distribution of centroid positions aligns with the mode of the exact (physical) quantum radial distribution along that coordinate.

Here we present an alternative procedure, that does not require running PIMD simulations. As discussed by Trenins and Althorpe in Ref. 69, for vibrational modes coupled to curvilinear motion, there is a temperature below which artificial instantons are likely to emerge for centroid-constrained ring-polymer configurations sampled by CMD. In order to determine this temperature, the authors of Ref. 69 have conveniently defined a crossover radius r_x . If the centroid position along a given radial coordinate lies below r_x , artificial instantons form, and both the shape and position of the vibrational peak are dramatically altered. There is a simple and general expression for r_x , found by assuming a single decoupled vibrational coordinate and minimizing the ring-polymer energy subject to the centroid constraint. This expression reads

$$r_x(\beta) \simeq -\frac{\beta}{2\mu\pi} \frac{\partial V(r - r_{eq})}{\partial r} \bigg|_{r=r_x}, \quad (10)$$

where μ is the (reduced) mass of the vibrational motion, V is the radial part of the potential along that coordinate and r_{eq} is the equilibrium position.

For our purposes, it is convenient to define three temperature regimes, according to how much of the centroid thermal distribution extends beyond r_x . The high-temperature regime ($T > T_{\text{high}}$) corresponds to a distribution with a negligible weight beyond r_x , as in the top panel of Fig. 3 in Ref. 69, which we reproduce in the SI Fig. S3. Here, the curvature problem is negligible and the elevated-temperature *ansatz* is dropped, so that the “elevated” and the physical temperatures can be kept equal, $T_e = T_{\text{phys}}$.

In the low-temperature regime ($T < T_{\text{low}}$), r_x substantially overlaps with the centroid distribution, as in the bottom panel of Fig. S3. This is linked to line shape deformation in standard PA-CMD and a growing deviation between the distribution modes for centroid and *quasicentroid* coordinates (the compact curvilinear coordinates introduced in Ref. 59 – also see Sec. I). In this regime, the curvature problem affects the centroid PMF even around equilibrium and should not be used for vibrational dynamics simulations. We, therefore, impose a lower bound on the elevated temperature, $T_e \geq T_{\text{low}}$.

In the intermediate temperature range, $T_{\text{low}} < T < T_{\text{high}}$, r_x overlaps a non-negligible part of the centroid distribution

(middle panel of Fig. S3), but is still far enough not to corrupt the PMF around the equilibrium geometry. When the physical temperature drops below T_{high} we propose to pick an elevated temperature $T_e > T_{\text{phys}}$ from this range. T_e should be as low as possible to fulfill the low-temperature criterion of Sec. II B but high enough for r_x to shift far away from the mean of the centroid thermal distribution $\mathcal{P}(r_c, \beta_{\text{phys}})$ computed for the PMF $\bar{U}(\mathbf{q}_c, \beta_e)$.

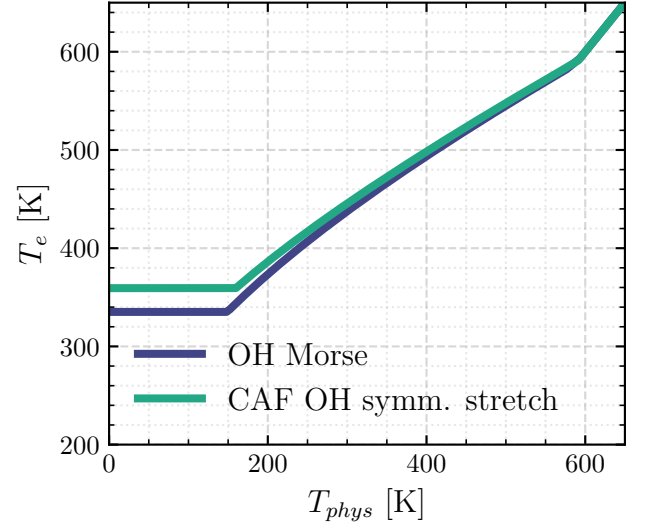


FIG. 1. Elevated temperature T_e as a function of the physical temperature T_{phys} for the analytical radial OH Morse potential with the same parameters as in Ref. 59 (blue) and for a numerically calculated symmetric OH stretch vibration of the carbonic acid fluoride (CAF) molecule discussed in this paper (green).

In polar coordinates, we are not aware of an analytical closed-form solution for the probability distribution of r_c on the centroid PMF of Eq. (4), even when the potential is harmonic in the radial coordinate. However, following from the argument in Sec. II B, at sufficiently low temperatures such that the system still remains at the vibrational ground state, but high enough that the ring polymer is not overly spread around the curvilinear potential energy profile, we can approximate the PMF as harmonic along this coordinate, leading to a linear force on r_c and a Gaussian thermal distribution. In other words, we consider

$$\mathcal{P}(r_c, \beta) \propto \exp[-\beta \mu \omega_{\text{harm}}^2 (r_c - r_{eq})^2], \quad (11)$$

where $\mu \omega_{\text{harm}}^2 = \partial^2 V(r - r_{eq}) / \partial r^2|_{r=r_{eq}}$. The standard deviation is

$$\sigma(\beta) = (\beta \mu \omega_{\text{harm}}^2)^{-1/2}. \quad (12)$$

More controlled approximations to this distribution can be considered in future work, e.g., based on steepest-descent integration of Eq. (4). This kind of analysis would account for the temperature-dependent shift in the mode of the distribution, which, in reality, is not strictly fixed at r_{eq} , as well as for anharmonicity along the radial coordinate. The quality of the

approximation we use indeed becomes less justified at very low temperatures. However, the current treatment is sufficient to get a robust estimate for an optimal T_e and has the added benefit of simplicity.

For our recipe, we numerically solve Eq. (10) for a given anharmonic $V(r_c)$ and define

$$T_{\text{high}} = 1/k_B\beta_{\text{high}} \quad \text{s.t.} \quad r_{eq} - r_x(\beta_{\text{high}}) = 6\sigma(\beta_{\text{high}}), \quad (13a)$$

$$T_{\text{low}} = 1/k_B\beta_{\text{low}} \quad \text{s.t.} \quad r_{eq} - r_x(\beta_{\text{low}}) = 4\sigma(\beta_{\text{low}}). \quad (13b)$$

The choice of multiples of σ in Eq. (13) is somewhat arbitrary but was found to give good results in our numerical tests.

To find the optimal elevated temperature in all regimes, we then invert the numerical solutions to Eq. (10) to obtain the crossover temperature for a given centroid radial displacement $\beta_x(r_c)$. For any physical temperature $T_{\text{phys}} < T_{\text{high}}$, we compute $\beta_e = \beta_x(r_{eq} - 6\sigma(\beta_{\text{phys}}))$. The elevated temperature T_e is then set to the largest of $1/k_B\beta_e$ and T_{low} . This choice is motivated by the fact that the approximation in Eq. (11) becomes worse at very low temperatures. Above T_{high} , we obviously set $T_e = T_{\text{high}}$. The procedure only requires the 1D potential-energy profiles of the vibrational motions that are prone to the curvature problem and, thus, gives a simple and general prescription for T_e .

For the 2D champagne-bottle potential widely studied in this context^{36,59,61,64,69}, the solutions for T_e at different physical temperatures T_{phys} are shown in Fig. 1. In the same figure, we show the solution for the symmetric OH stretch of the CAF molecule that we mapped numerically, as an example of an anharmonic vibrational motion where the curvature problem is very pronounced. We observe that the curvature problem disappears at around $T_{\text{high}} \approx 600$ K, and that our procedure allows us to select $T_e < T_{\text{high}}$ tailored to specific physical temperatures. Numerical tests on the water monomer, CAF, and MAPI presented in Section 3 of the SI validate this procedure.

D. Implementing Partially-Adiabatic CMD with the Elevated Temperature Ansatz

The original implementation of elevated-temperature CMD is called T_e -PIGS.⁶⁴ In that approach, the centroid force is extracted from high-temperature path-integral simulations, and a machine-learned interatomic potential (MLIP) is subsequently trained to approximate the PMF at T_e by using path-integral coarse-graining techniques. T_e -PIGS offers accuracy and efficiency advantages. The dynamics are accurate (within the approximations of the method) because there is a strict adiabatic separation of the centroid and the internal modes of the ring polymer and they are efficient because one simply performs classical molecular dynamics on the pre-trained centroid PMF.

One of the main drawbacks is the setup overhead: the centroid PMF is a free-energy surface that must be parameterized separately, often by combining a baseline ML interatomic potential with an additional model, which introduces extra training steps, even compared to using a standard MLIP. This can make T_e -PIGS cumbersome for systems whose relevant free-energy landscape spans many distinct configurations that may

differ considerably from those sampled at the elevated training temperature, and for systems where current ML potentials are not sufficiently accurate.

The partially adiabatic formulation of elevated-temperature CMD (PA- T_e -CMD) addresses these drawbacks. PA- T_e -CMD computes the centroid PMF on the fly, eliminating the need for precomputed PMFs. This is achieved by implementing a two-temperature path-integral Langevin equation thermostat (2T-PILE). The 2T-PILE thermostat extends the standard path-integral Langevin equation (PILE) thermostat to simultaneously thermalize the centroid at the target temperature T_{phys} while equilibrating the internal modes at the elevated temperature T_e .

The 2T-PILE formulation follows the general structure of PILE thermostats,⁶⁷ introducing stochastic and dissipative forces for each normal mode k of the ring polymer,

$$\tilde{p}_{(k)} \leftarrow c_{1,(k)}\tilde{p}_{(k)} + \sqrt{\frac{m}{\beta_{(k)}}}c_{2,(k)}\xi_{(k)}, \quad (14)$$

where $\xi_{(k)}$ is Gaussian white noise with zero mean and unit variance. The coefficients $c_{1,(k)}$ and $c_{2,(k)}$ are defined as:

$$c_{1,(k)} = \exp\left[-\frac{\Delta t}{2}\gamma_{(k)}\right], \quad c_{2,(k)} = \sqrt{1 - (c_{1,(k)})^2}. \quad (15)$$

The friction coefficients are defined by

$$\gamma_{(k)} = \begin{cases} \frac{1}{\tau_0}, & k = 0, \\ \lambda 2\omega_k\sigma_k, & k > 0, \end{cases} \quad (16)$$

where ω_k is the frequency of the ring-polymer mode k and σ_k is the partially adiabatic scaling parameter in Eq. (7). The parameter λ controls the degree of damping of the internal ring-polymer modes by the Langevin thermostats, whereas τ_0 governs the relaxation time of the thermostat attached to the centroid.

Compared to the standard setup, 2T-PILE only modifies the temperature entering Eq. (14). It assigns distinct inverse temperatures $\beta_{(k)}$ to normal modes with the index k ,

$$\beta_{(k)} = \begin{cases} \frac{1}{k_B T_{\text{phys}}}, & k = 0, \\ \frac{1}{k_B T_e}, & k > 0, \end{cases} \quad (17)$$

so that the adiabatically separated fluctuation modes sample the thermodynamic ensemble consistent with T_e , while the centroid evolves on the resulting PMF at a temperature T_{phys} . We stress that the ring polymer springs are defined such that they are consistent with the elevated temperature as well, i.e., $\omega_k = 2P/(\beta_e\hbar)\sin(k\pi/P)$.

As discussed in Ref. 41, for PA-CMD protocols, the parameter λ needs to remain in the under-damped regime to minimize artificial coupling between internal and centroid modes. Moreover, in usual PA-CMD protocols, one sets τ_0 to be very large, effectively switching off the centroid thermostat. This is done to minimize the disturbance to the centroid dynamics,

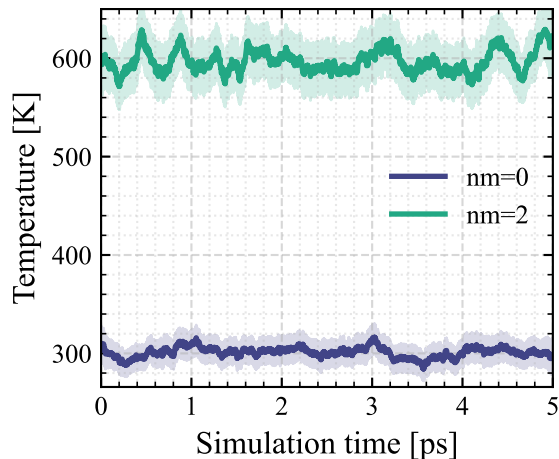


FIG. 2. Time evolution of the temperatures of the centroid mode ($nm=0$, blue line) and the second internal normal mode of the ring polymer ($nm=2$, green line) during a $PA-T_e$ -CMD simulation of an isolated water monomer at $T_{\text{phys}} = 300$ K and $T_e = 600$ K. Solid lines show centered moving averages, and shaded areas indicate the 95% confidence intervals computed from a moving window. Both modes exhibit stable and distinct temperatures throughout the simulation, as expected from the 2T-PILE thermostat.

ensuring the correct evaluation of time-correlation functions according to Eq. (3).

In $PA-T_e$ -CMD, we found that a weak global thermostat attached to the centroid helps prevent kinetic energy leakage from internal ring-polymer modes. To achieve this, instead of using a local Langevin thermostat attached to the centroid mode like in Eqs. (14) and (16), we adopt the same strategy as in Ref. 67 and attach instead a “global” thermostat to the centroid, that acts on the kinetic energy of the system, instead of the individual momenta. This thermostat is the stochastic velocity rescaling (SVR) thermostat,⁷⁴ which only minimally disturbs dynamics if its relaxation time, which we will call τ , is not too small.

We have implemented this thermostat in the i-PI program package.⁷⁵ Figure 2 illustrates the action of the 2T-PILE thermostat with $T_e = 600$ K and $T_{\text{phys}} = 300$ K for an isolated water monomer. It shows the successful independent thermalization of the centroid and non-centroid modes at distinct temperatures. We benchmark the performance of different λ and τ parameters in Section IV A.

III. COMPUTATIONAL DETAILS

This section details the computational protocols employed in our $PA-T_e$ -CMD and T_e -PIGS simulations for three representative systems: a water monomer, the carbonic acid fluoride (CAF) molecule and the methylammonium lead iodide (MAPI) perovskite. These systems were selected to assess the performance and limitations of our method across diverse vibrational environments. The water monomer serves as a benchmark due to its well-characterized vibrational spectrum

and the availability of exact quantum reference data. CAF presents strong anharmonicity for some vibrational motions, related to the presence of a strong ionic hydrogen bond. Finally, MAPI presents mild anharmonicity, but exhibits multiple polymorphs across different temperatures.

We employed the following interatomic potentials for each system: (i) the Partridge–Schwenke potential⁷⁶ for the water monomer; (ii) a MACE^{77,78} potential trained on density-functional theory data using the B3LYP functional^{79,80} and including pairwise dispersion interactions⁸¹ for CAF; and (iii) a MACE potential trained on density-functional theory data using the HSE06^{82,83} hybrid range-separated functional and incorporating many-body dispersion interactions⁸⁴ for MAPI.

All $PA-T_e$ -CMD simulations were run with the i-PI code⁷⁵. For comparison, vibrational spectra were also computed using classical molecular dynamics, thermostatted ring-polymer molecular dynamics (TRPMD), partially-adiabatic centroid molecular dynamics (PA -CMD) and T_e -PIGS, using the i-PI code as well. The T_e -PIGS simulations were performed following the methodology of Ref. 7 and utilized the same baseline potentials as $PA-T_e$ -CMD for each system. The T_e -PIGS centroid potential of mean force was trained with $T_e = 600$ K for the water monomer, for comparison with previous work⁶⁴. For MAPI, the PMF for T_e -PIGS was trained at $T_e = 500$ K and at the cubic phase. Finally, for CAF we used PMF trained at several temperatures, as discussed below. Further computational details on the elevated-temperature simulations, as well as on the additional simulation methods, are provided in Sections 4 and 5 of the SI.

IV. RESULTS

A. Benchmarks on the Water Monomer

We start by benchmarking the $PA-T_e$ -CMD method for the water monomer. Fig. 3 shows the O–H bending (1100 – 2000 cm^{-1}) and stretching (3500 – 4200 cm^{-1}) vibrational bands in the IR spectrum of the water monomer. We show exact spectra obtained via discrete variable representation (DVR) on the same potential, which we take as the reference, and $PA-T_e$ -CMD with a combination of different τ and λ parameters, discussed in Section II D.

We tested the following parameter values: $\tau = 10, 20, 100$ fs and $\lambda = 0.01, 0.001$. The adiabatic separation frequency was fixed at $\Omega = 24000$ cm^{-1} . These values were chosen to explore the tradeoffs between thermostat strength, sampling efficiency, and spectral accuracy. Smaller τ values introduce larger disturbances to the dynamics of the centroid, but maintain its temperature more efficiently, while smaller λ values drive the dynamics of non-centroid modes in the strongly underdamped regime, which tends to decrease the thermostat efficiency, but also decrease spurious coupling to the high-frequency physical modes.

Figure 3a–c compares $PA-T_e$ -CMD spectra across five combinations of the parameters τ and λ , benchmarked against the exact DVR reference. For future reference, we label them as follows: Set A ($\tau = 10$ fs, $\lambda = 0.01$), Set B ($\tau = 10$ fs,

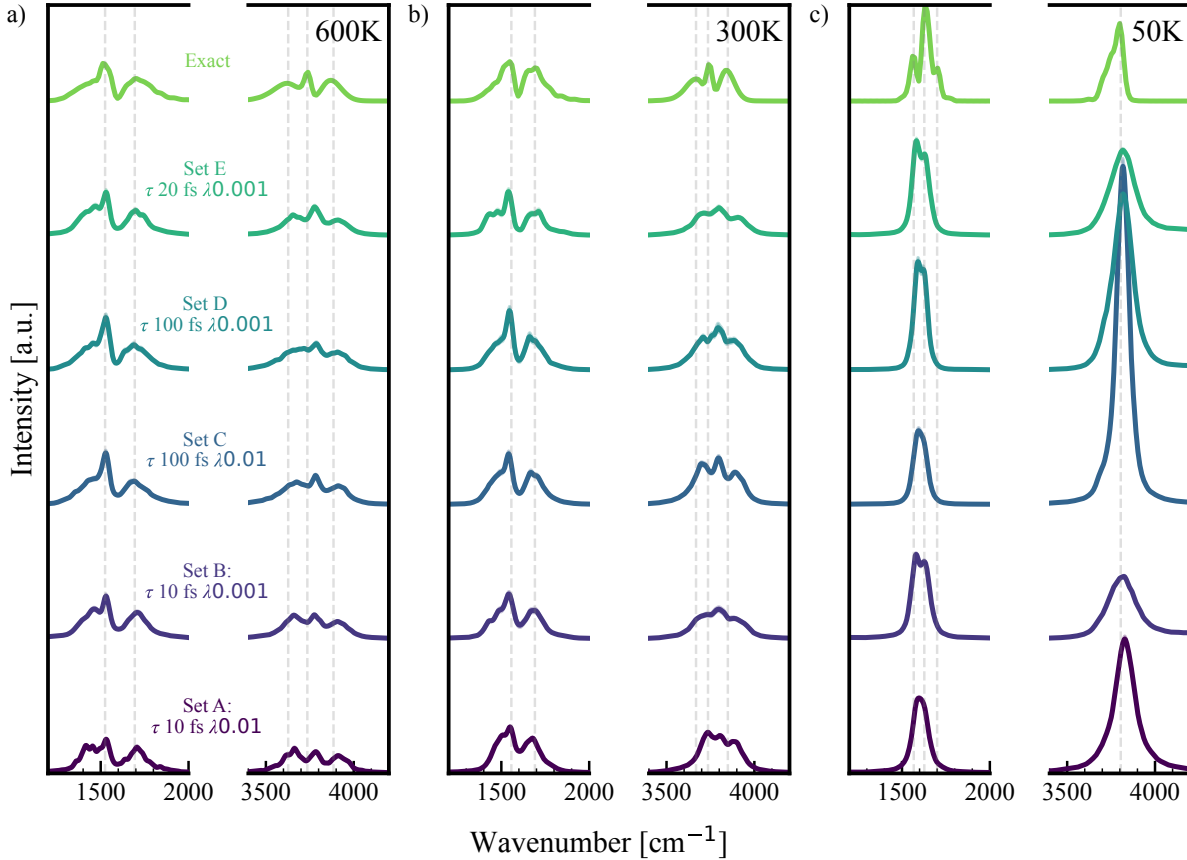


FIG. 3. Bending (1100–2000 cm^{-1}) and O–H stretching (3500–4200 cm^{-1}) infra-red vibrational bands of a water monomer obtained via PA- T_e -CMD with five parameter sets compared to the DVR reference at 600 K, 300 K, and 50 K.

$\lambda = 0.001$), Set C ($\tau = 100$ fs, $\lambda = 0.01$), Set D ($\tau = 100$ fs, $\lambda = 0.001$), and Set E ($\tau = 20$ fs, $\lambda = 0.001$). We kept the elevated temperature at $T_e = 600$ K in this case, for comparison with the benchmarks carried out in Ref. 64. Therefore, we used 16 beads for PA- T_e -CMD at all temperatures.

We evaluated the performance of each spectrum using the Earth Mover’s Distance (EMD)⁸⁵ as a quantitative metric of spectral similarity. Benchmarking and validation of this metric are provided in Section S6 of the Supplementary Information, together with the numerical values in Table S4. By construction, a lower EMD indicates better agreement. For this system, spectra with EMD values within ~ 80 units are qualitatively indistinguishable, while values exceeding 250 units correspond to clear, visually detectable deviations. Because of the presence of small-amplitude oscillations in the spectra, the threshold for what constitutes a “sufficiently low” EMD can vary somewhat with temperature.

At 600 K (Figure 3a), all parameter sets reproduce the DVR frequencies and capture the key spectral features, despite their EMD values ranging from 46 (Set E) to 98 (Set D). Among them, Set E (EMD = 47) provides the best agreement, followed by Set A (EMD = 55).

At 300 K (Figure 3b), Set E again performs best (EMD

= 35), followed by Set B (EMD = 83). In contrast, Set A (EMD = 269) and Set C (EMD = 275) show more significant deviations across the vibrational features, in line with their much larger EMD scores.

At 50 K (Figure 3c), all parameter sets avoid the curvature problem, but the spectral lineshapes deteriorate due to a slight overheating of the stretch modes. This heating originates from kinetic energy leakage from the internal ring-polymer modes to the centroid, and becomes particularly severe when $\tau = 100$ fs is used, as it fails to maintain the lower centroid temperature. At this temperature, Set B (EMD = 552) and Set E (EMD = 711) provide the most reasonable agreement, while Sets A, C, and D yield EMD values above 1000, consistent with visibly poorer spectra.

These results establish Set B and Set E ($\tau = 10, 20$ fs, $\lambda = 0.001$) as the most robust parameter choices across all temperatures (Table S4). We therefore employ these sets in the subsequent comparisons with alternative approaches. We note that reducing T_e (e.g., to 350 K) helps mitigate energy leakage into the OH stretch band at low temperatures (Figure S3), and could permit slightly larger values of τ .

Figure 4 compares PA- T_e -CMD (Set E) with T_e -PIGS, standard CMD, TRPMD, and classical MD at all three tempera-

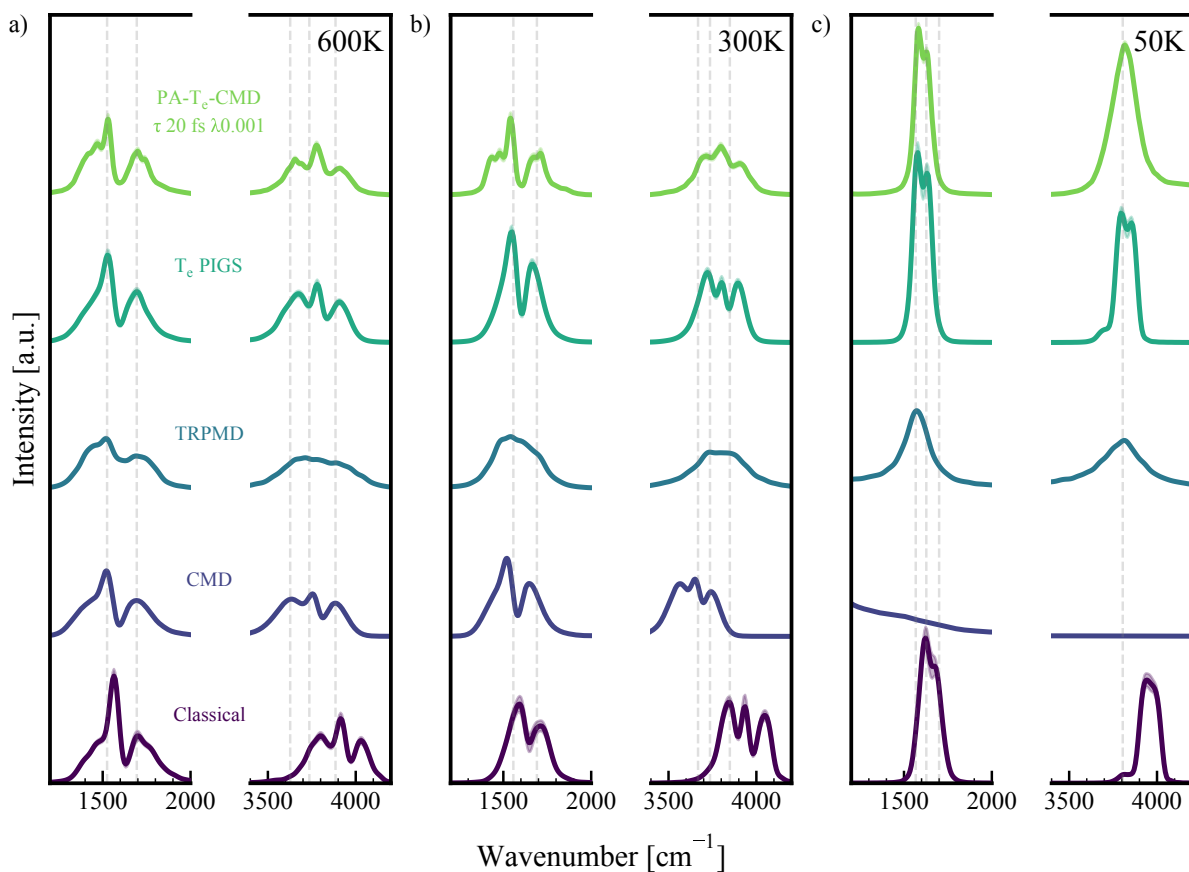


FIG. 4. Comparison between PA- T_e -CMD (Set E), T_e -PIGS, standard CMD, TRPMD, and classical MD against the DVR reference for bending (1100–2000 cm^{-1}) and O–H stretching (3500–4200 cm^{-1}) IR vibrational bands of a water monomer at 600 K, 300 K, and 50 K.

tures, using the DVR spectrum as a reference, displayed as gray vertical lines at the position of the vibrational peaks. PA- T_e -CMD accurately captures vibrational peak positions across the temperature range, reproducing the quantum red-shift without the overbroadening seen in TRPMD or the spurious curvature-induced redshift of CMD. Its performance closely tracks that of T_e -PIGS. A slight thermal broadening and intensity increase of the PA- T_e -CMD peaks is observed at 50 K, due to the kinetic-energy leakage mentioned above. This broadening is far smaller than the TRPMD spectrum at the same temperature.

B. Vibrational Fingerprints of Strongly Anharmonic Vibrations in the Carbonic Acid Fluoride

Carbonic acid was shown to form a surprisingly stable complex with fluoride atoms in the gas phase, in which strong ionic hydrogen bonds are involved⁸⁶. These bonds in the carbonic acid fluoride $[\text{H}_2\text{CO}_3\text{F}]^-$ (CAF) molecular complex were shown to exhibit strongly anharmonic dynamics, characterized by fingerprints of its measured and simulated IR spectrum in the OH-stretch region⁸⁶. The most stable conformer is of C_{2v} symmetry, with the fluoride sitting equidistant to both

OH groups. Here, we revisit this problem from a simulation perspective and show the performance of different flavours of TRPMD and CMD for the vibrational spectrum.

Figure 5 presents the vibrational density of states (VDOS) for CAF computed at 100 K using T_e -PIGS ($T_e = 350$ K), PA- T_e -CMD ($T_e = 350$ K), TRPMD, TRPMD+GLE³⁷, CMD and classical MD. It should be noted that the comparison to experiment is here rather qualitative, as the experimental data corresponds to IR active bands at the cryogenic temperature of 0.4 K⁸⁶, which is impractical for explicit path-integral methods. We prefer to show the full VDOS spectrum for the methodological comparison and note that the calculation of the IR spectrum would not change our conclusions.

In the region below 2000 cm^{-1} , all methods yield a fairly similar spectrum. In particular, all methods that include nuclear quantum effects predict a slight blue-shift of the bands labeled 1 (F^- displacement wrt. carbonic acid) and a slight red-shift of the band labeled 9 (CO stretch coupled to OH bend in-plane bend), with respect to the f1 and f9 bands in the classical-nuclei spectrum. In both cases, this leads to a better agreement with experiment. The TRPMD spectrum presents the largest (spurious) broadening of all peaks, as expected for this method. The bands labeled 6, 7 and 8, comprising C out-of-plane displacement, CO in-plane stretches and OH in and

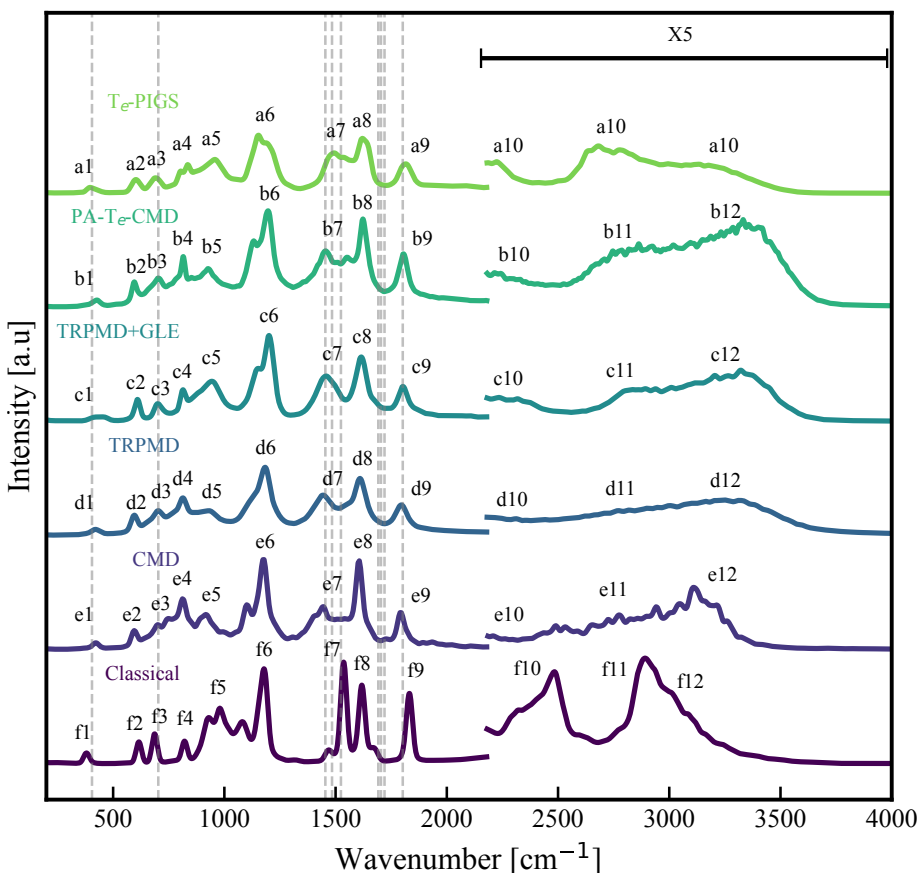


FIG. 5. Vibrational density of states (VDOS) of carbonic acid fluoride (CAF) at 100 K, computed using (from top to bottom) T_e -PIGS, PA- T_e -CMD, TRPMD+GLE, TRPMD, CMD, and classical MD. $T_e = 500$ K for T_e -PIGS and PA- T_e -CMD. Experimental IR bands are shown as gray dashed lines. The molecular structure of CAF is shown on the right. Atom color code: oxygen (red), hydrogen (white), carbon (brown), and fluorine (light blue).

out-of-plane bends are very similar in PA- T_e -CMD, CMD, TRPMD and TRPMD+GLE. T_e -PIGS also produces a fairly similar spectrum to the other methods in this region, but with a narrower 7/8 band, which comprises OH in-plane bending motion. The similarity among these methods strongly suggests that spectral broadening is primarily driven by anharmonic coupling.

In the region above 2000 cm^{-1} , dominated by symmetric and anti-symmetric OH stretch vibrations, the PA- T_e -CMD, TRPMD and TRPMD+GLE yield broad spectral features, labeled 10, 11 and 12, with a substantial spectral weight above 3000 cm^{-1} , consistent with the anharmonic blue-shift previously reported for this system⁸⁶. CMD also exhibits a high-frequency band, but unlike the other methods, it appears red-shifted and slightly more broadened than its PA- T_e -CMD counterpart — a signature of the curvature problem. To disentangle the contributions of the curvature problem and kinetic energy leakage to the broadening of the OH stretching bands, we performed a T_e -scan using PA- T_e -CMD, shown in Figure S5 (SI). The redshift characteristic of the curvature problem is largely absent already at $T_e = 350$ K; however, the bands remain broad. Since further increasing T_e up to 500 K does not significantly affect the lineshape, this suggests that the ob-

served broadening arises predominantly from the anharmonic dynamics. T_e -PIGS predicts a different spectral weight of the bands in this region. We will see that this is related to the PMF that was used.

We trained PMFs for T_e -PIGS at 500, 400 and 350 K. We observed that at 500 K an HF molecule forms and promptly dissociates, such that only a few structures of the bound molecule can be obtained from the PIMD simulations. This could be caused by inaccuracies in the underlying MLIP, but this is a low-energy structure that was discussed in Ref. 86 for this complex. Computing a T_e -PIGS spectrum with a PMF trained on this data leads to a spectrum that looks very much like the classical one, but with red-shifted high-frequency bands, in disagreement with all other methods (see Figure S10). Decreasing the temperature allows the molecule to stay bound for longer and improves the resulting spectral shape obtained by T_e -PIGS. However, the spectral weights on bands 11 and 12 are in slight disagreement with the other methods, likely due to challenges in sampling appropriate centroid configurations for fitting the PMF that are locally similar to those at the lower temperatures. For systems that are weakly bound and reactive, PA- T_e -PIGS can thus offer a more robust alternative, as it samples the local PMF on-the-

fly and more faithfully. In addition, PA- T_e -PIGS may benefit from some error cancellation, as some energy leakage from the internal modes could increase the spectral weight of the peak labeled 12.

To better understand how anharmonic coupling induces spectral broadening, we analyzed the free energy surfaces (FES) along the O–H and H \cdots F $^-$ displacement coordinates (Figure S11). The FES obtained with PA- T_e -CMD and TRPMD+GLE are broad, allowing the proton to explore large regions of the potential energy surface at minimal energetic cost (see also Figure S12). The FES regions explored by the proton in the classical-nuclei simulations are much narrower. The greater mobility in the quantum simulations allows the system to access configurations where the hydrogen–fluorine distances substantially exceed typical hydrogen-bonding lengths, resulting in a loss of the double hydrogen bond present in the optimized structure. Visual inspection confirms that these are structures wherein one O–H group forms a strong single hydrogen bond with fluorine, elongating the bonded O–H, while the other O–H group contracts due to the lack of direct hydrogen-bonding interactions. It is interesting to note that these structures, which break the C_{2v} symmetry, resemble other stable low-energy minima of CAF discussed in Ref. 86. The presence of the free OH group gives rise to the blue-shifted band in the quantum spectra. In the classical simulations, the F $^-$ anion largely remains equally shared between the two OH groups.

C. Nuclear Quantum Effects in the Vibrational Spectra of Different Phases of Methylammonium Lead Iodide (MAPI)

After assessing the performance of PA- T_e -CMD on the water monomer and the CAF molecular complex, we move to the analysis of the vibrational spectrum of the hybrid organic-inorganic perovskite MAPI. The vibrational features of MAPI in its various phases have been studied with the purpose of phase characterization^{87,88}, determination of the rotational and reorientation dynamics of organic cations (methylammonium)^{87,89}, and understanding of anharmonic lattice vibrations related to its low thermal conductivity^{90–92}. Here, we assess the impact on nuclear quantum effects in its vibrational spectrum, as predicted by the various flavors of CMD.

Fig. 6 shows the vibrational density of states (VDOS) of MAPI in the tetragonal phase at 300 K (a) and the orthorhombic phase at 110 K (b), computed using T_e -PIGS ($T_e = 500$ K), PA- T_e -CMD ($T_e = 400$ K), standard CMD, and classical MD. The vibrational spectrum of MAPI is typically divided into three regions: (1) low-frequency internal vibrations of the PbI₃ network (<100 cm $^{-1}$), (2) methylammonium (MA) cation librations (140–180 cm $^{-1}$), and (3) internal vibrations of the MA cation (800–3100 cm $^{-1}$)⁸⁷. Our analysis focuses on the third region, where experimental IR data are available for direct comparison. Experimental IR peak positions from Ref. 93 are shown as vertical gray lines.

At both temperatures, T_e -PIGS and PA- T_e -CMD exhibit good agreement with the experimental IR spectrum, with most experimental peaks falling within 10 cm $^{-1}$ of the computed

ones. However, deviations of up to 45 cm $^{-1}$ are observed, particularly for features associated with the C–N stretching mode (labeled 2). At 300 K, PA- T_e -CMD overestimates this mode by 30 cm $^{-1}$, similar to T_e -PIGS. At 110 K, deviations increase to 44 cm $^{-1}$ for PA- T_e -CMD and 38 cm $^{-1}$ for T_e -PIGS. Interestingly, classical MD spectra show similar separations between peaks c1/c2 (300 K) and g1/g2 (110 K), suggesting that the discrepancies originate not from the quantum methods, but rather from limitations in the underlying potential, likely related to the level of theory used to train the neural network.

The role of NQEs was assessed by comparing quantum (T_e -PIGS, PA- T_e -CMD) and classical MD spectra at 300 K. As expected, NQEs are most prominent in the high-frequency region, where the zero-point energy (ZPE) of hydrogen atoms plays a dominant role. For the symmetric N–H stretching mode (labeled 8), redshifts of 83 cm $^{-1}$ (10.4 meV) and 79 cm $^{-1}$ were observed with T_e -PIGS and PA- T_e -CMD, respectively. The asymmetric N–H stretch (labeled 9) exhibited even larger redshifts of 94 cm $^{-1}$ (11.7 meV) and 85 cm $^{-1}$. Bending modes also showed noticeable redshifts, up to 38 cm $^{-1}$ for T_e -PIGS and 44 cm $^{-1}$ for PA- T_e -CMD. In contrast, modes dominated by heavier atoms—such as the C–N stretch and CH₃NH₃ rocking motions (features 1 and 2)—exhibited much smaller shifts (~ 9 cm $^{-1}$). Similar trends were observed at 110 K, with quantum effects becoming more pronounced at lower temperatures.

The comparison with CMD is particularly revealing at 110 K, where the curvature problem becomes evident. Features d2 to d9 in T_e -PIGS and e2 to e9 in PA- T_e -CMD are consistently blue-shifted relative to CMD frequencies. In CMD, spurious redshifts and broadening suppress the separation of N–H stretching and C–H stretching, merging them into a single band due to different curvatures of the potential energy. The curvature problem also alters the lineshape, suppressing the asymmetric N–H bending modes (d6 and e6 in the elevated-temperature methods), which merge into a single feature (f5/6) in CMD.

Overall, the T_e -PIGS spectra align closely with the PA- T_e -CMD spectra, both in position and lineshape. However, in the low-temperature orthorhombic phase, noticeable discrepancies emerge in the high-frequency NH stretching region: the PA- T_e -CMD spectra are broader and slightly less resolved compared to their T_e -PIGS counterparts. This broadening is attributed to the coupling between physical high-energy modes and the hot non-centroid ring-polymer modes. As shown in Figure S6, this artifact is mitigated by lowering the elevated temperature even further. However, lowering T_e below 350 K reintroduces the curvature problem and deteriorates the spectral accuracy in the low-temperature regime, as expected from our analysis in Section II C.

We note that the orthorhombic phase, in particular, exhibits highly anharmonic energy profiles along the NH stretching coordinates, as discussed in Section 8 of the Supplementary Information. These non-negligible anharmonic coefficients induce stronger coupling between the centroid and internal ring-polymer modes. While PA- T_e -CMD partially suppresses this coupling through the adiabatic separation, it is to be ex-

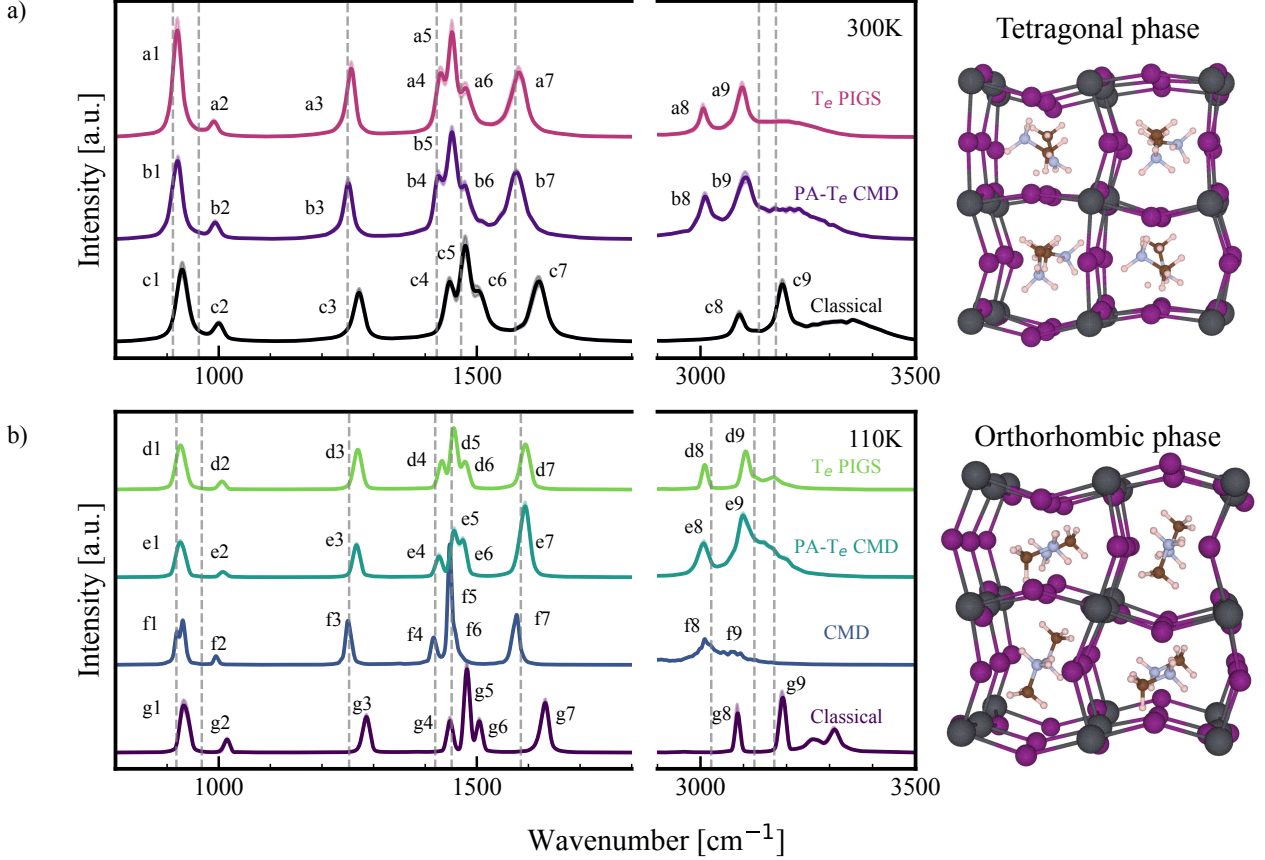


FIG. 6. Vibrational density of states (VDOS) of MAPI computed using T_e -PIGS, PA- T_e -CMD, CMD, and classical MD. (a) Tetragonal phase at 300 K. (b) Orthorhombic phase at 110 K. Experimental IR peak positions are shown as vertical dashed lines for reference. The computed spectra are shifted vertically for clarity. The right panels show the corresponding crystal structures: lead atoms in dark gray, iodine in purple, carbon in brown, nitrogen in light blue, and hydrogen in white.

pected that spurious effects due to energy exchange between “hot” and “cold” modes of the ring polymer are more pronounced at the orthorhombic phase.

Finally, we draw attention to the fact that PA- T_e -CMD and T_e -PIGS largely agree for the tetragonal and orthorhombic phases of this system, even when the T_e -PIGS PMF was parametrized at the high temperature cubic phase. Therefore, we can conclude that this method is generally successful in capturing NQE across material phases, presumably as long as the potential energy profile of the high-frequency vibrations is not very altered in different phases⁹⁴. As shown in Section 9 of the SI, we also investigated the changes on high-frequency OH stretch peaks of liquid water induced by pressure, as a stringent test of this transferability. While the shifts in peak positions are very small when varying the pressure at the accessible experimental range, PA- T_e -CMD seems to capture the shift in the right direction. T_e -PIGS only successfully captures the trend in peak shifts when using elevated temperature PMFs trained at each respective pressure. However, because these changes are extremely small, we refrain from making a strong statement in this respect. In any case, it is plausible that training a general machine-learned PMF for T_e -PIGS that

is aware of several different material phases will make that method more accurate.

V. CONCLUSIONS

The findings discussed in this paper reinforce the applicability of the elevated-temperature *ansatz* in centroid molecular dynamics as an accurate framework for including nuclear quantum statistics in vibrational spectroscopy. Compared to the original T_e -PIGS implementation, the method developed in this work, the partially-adiabatic PA- T_e -CMD, enhances transferability and makes the method simpler to use by eliminating the need for coarse-grained PMFs. This method emerges as a promising alternative for accurate vibrational calculations suitable for systems with significant configurational flexibility and reactivity, such as molecular complexes, biomolecules, and materials near phase transitions.

The benchmarks we have carried out showed that the thermostat parameters used in PA- T_e -CMD can have a substantial effect on the resulting vibrational spectra. Here, we have explored different parameter regimes of the 2T-PILE thermostat,

introduced in Section II D. The λ parameter, which controls the degree of damping of Langevin thermostats coupled to the non-centroid ring-polymer modes can be safely chosen in the underdamped regime, with $\lambda = 0.001$ being optimal for minimizing spurious features on the spectra. The parameters of the thermostat acting on the centroid are also crucial for accurate temperature control in PA- T_e -CMD simulations. PA- T_e -CMD requires stronger coupling to prevent unwanted energy transfer between the centroid and non-centroid modes. Especially at low temperatures, a smaller thermostat relaxation time τ of 10-20 fs performs best. For example, in the water monomer at 50 K, larger τ allows kinetic energy to leak from ring-polymer internal modes to the high-frequency physical vibrational modes, distorting the vibrational spectrum.

The selection of the elevated temperature T_e is equally critical. It must be high enough to mitigate curvature issues while ensuring that high-frequency normal modes, which are most affected by nuclear quantum effects (NQE), remain in their quantum ground state. We have devised a practical procedure for choosing T_e at different physical temperatures, and confirmed that values of T_e between 350 and 600 K are effective for this method. The optimal value of T_e will depend both on the anharmonic profile of the high-frequency vibrational modes and the physical temperature desired. For PA- T_e -CMD, choosing the optimal elevated temperature can be crucial, as being able to choose a lower T_e for simulations at lower physical temperatures decreases thermal energy leakage from the internal modes to the centroid.

The two elevated-temperature approaches, PA- T_e -CMD and T_e -PIGS, exhibit distinct strengths depending on the system. T_e -PIGS is completely adiabatic, but requires a precomputed centroid PMF, which can be computationally demanding to obtain and which can contain fitting errors. Generating a new PMF requires additional data collection and reparameterization, making it more demanding for applications where thermodynamic conditions change. By contrast, PA- T_e -CMD eliminates the need for precomputed PMFs and instead computes the centroid PMF on-the-fly, reducing the setup complexity. However, PA- T_e -CMD incurs a higher per-step cost due to the small time-step necessary to propagate the equations of motion and can suffer from energy leakage. In terms of computational cost, PA- T_e -CMD is roughly an order of magnitude more expensive than TRPMD, primarily due to the smaller time step required to maintain adiabatic separation. Its cost is comparable but smaller than standard PA-CMD, as one needs typically only 8-16 beads to run the simulations at a given T_e , for any physical temperature. In contrast, once a suitable machine-learned PMF is available, T_e -PIGS offers the fastest dynamics, as it allows for classical time steps and eliminates the need for ring-polymer propagation altogether.

In analyzing vibrational spectra for systems containing multiple atomic species and a varied vibrational landscape, we conclude that both PA- T_e -CMD and T_e -PIGS efficiently remove the curvature problem of different curvilinear modes in molecular and condensed-phase systems. For the CAF molecule, we have clarified the dynamical motions that induce a blue-shifted OH stretching peak when including nuclear quantum effects. From a methodological perspective,

the strongly anharmonic nature of some vibrational modes and the higher reactivity of CAF makes it challenging to train a reliable PMF for T_e -PIGS. In this case, PA- T_e -CMD indeed presents a more reliable setup. On the other hand, PA- T_e -CMD and T_e -PIGS yield very similar vibrational spectra of MAPI tetragonal and orthorhombic phases, with a single PMF trained at the high-temperature cubic phase, and nuclear quantum effects bring the spectra closer to experimental data.

PA- T_e -CMD currently struggles in systems with strong anharmonicity of the PES and low temperature regimes, where the two-temperature thermostat we currently use is unable to maintain the temperature separation between centroid and non-centroid modes. Making PA- T_e -CMD spectra more accurate at lower-temperatures and for highly anharmonic systems will require the development of more advanced thermostating strategies, such as extending the two-temperature thermostating *ansatz* to generalized Langevin equation thermostats tailored for path-integral simulations.

The implementation of PA- T_e -CMD is already available in the i-PI code, requiring only a few additional parameter inputs compared to CMD and TRPMD. This streamlined setup makes it more accessible to general users and allows for direct coupling to existing *ab initio* or ML force calculators. Overall, we confirm that different flavors of elevated-temperature approaches mitigate artifacts inherent to CMD and TRPMD, enhance spectral accuracy, and increase efficiency of simulations. While T_e -PIGS is preferred when a reliable machine-learned PMF is available, particularly in strongly anharmonic regimes, PA- T_e -CMD provides a flexible and user-friendly alternative in scenarios where training such a model is impractical or data are scarce. Our study clarifies the trade-offs between these two implementations and highlights the broader applicability of elevated-temperature path-integral techniques in quantum vibrational spectroscopy.

REFERENCES

- ¹T. Ikeda, Chemical Physics Letters **763**, 138222 (2021).
- ²T. Ikeda, Chemical Physics Letters **811**, 140252 (2023).
- ³Y. Litman, J. O. Richardson, T. Kumagai, and M. Rossi, Journal of the American Chemical Society **141**, 2526 (2019).
- ⁴Y. Litman, J. Behler, and M. Rossi, Faraday Discuss. **221**, 526 (2020).
- ⁵M. Li, J. Kong, P. Wang, J. Lan, Y. Su, and J. Zhao, The Journal of Physical Chemistry Letters **16**, 3004 (2025).
- ⁶O. Marsalek and T. E. Markland, The Journal of Physical Chemistry Letters **8**, 1545 (2017).
- ⁷V. Kapil, D. P. Kovács, G. Csányi, and A. Michaelides, Faraday Discussions **249**, 50 (2024).
- ⁸M. Rossi, The Journal of Chemical Physics **154**, 170902 (2021).
- ⁹R. Rashmi and F. Paesani, Journal of the American Chemical Society **147**, 1903 (2025).
- ¹⁰V. Kapil and E. A. Engel, Proceedings of the National Academy of Sciences **119**, e2111769119 (2022).
- ¹¹S. Shepherd, G. A. Tribello, and D. M. Wilkins, The Journal of chemical physics **158** **20** (2023).
- ¹²R. Rashmi, T. O. Balogun, G. Azom, H. Agnew, R. Kumar, and F. Paesani, ACS Nano **19**, 4876 (2025), pMID: 39835751, <https://doi.org/10.1021/acsnano.4c16486>.
- ¹³M. Jarrell and J. Gubernatis, Physics Reports **269**, 133 (1996).
- ¹⁴A. Nakayama and N. Makri, The Journal of Chemical Physics **119**, 8592 (2003).

- ¹⁵J. A. Poulsen, G. Nyman, and P. J. Rossky, *The Journal of Chemical Physics* **119**, 12179 (2003).
- ¹⁶H. Wang and M. Thoss, *The Journal of Chemical Physics* **119**, 1289 (2003).
- ¹⁷H. Wang, *The Journal of Physical Chemistry A* **119**, 7951 (2015).
- ¹⁸H.-D. Meyer, U. Manthe, and L. Cederbaum, *Chemical Physics Letters* **165**, 73 (1990).
- ¹⁹N. Makri, *International Journal of Quantum Chemistry* **115**, 1209 (2015).
- ²⁰Y. Tanimura, *Phys. Rev. A* **41**, 6676 (1990).
- ²¹J. M. Bowman, *J. Chem. Phys.* **68**, 608 (1978).
- ²²K. Yagi, T. Taketsugu, K. Hirao, and M. S. Gordon, *The Journal of Chemical Physics* **113**, 1005 (2000).
- ²³J. Kongsted and O. Christiansen, *The Journal of Chemical Physics* **125**, 124108 (2006).
- ²⁴J. Bowman, T. Carrington, and H.-D. Meyer, *Mol. Phys.* **106**, 2145 (2010).
- ²⁵R. P. Feynman, A. R. Hibbs, and D. F. Styer, *Quantum mechanics and path integrals* (Courier Corporation, 2010).
- ²⁶M. Parrinello and A. Rahman, *The Journal of Chemical Physics* **80**, 860 (1984).
- ²⁷D. Chandler and P. G. Wolynes, *The Journal of Chemical Physics* **74**, 4078 (1981).
- ²⁸S. Bonella, M. Monteferrante, C. Pierleoni, and G. Ciccotti, *The Journal of Chemical Physics* **133**, 164104 (2010), https://pubs.aip.org/aip/jcp/article-pdf/doi/10.1063/1.3493448/13520970/164104_1_online.pdf.
- ²⁹L. Mühlbacher and E. Rabani, *Phys. Rev. Lett.* **100**, 176403 (2008).
- ³⁰G. Ilk and N. Makri, *The Journal of Chemical Physics* **101**, 6708 (1994).
- ³¹J. Cao and G. A. Voth, *The Journal of Chemical Physics* **100**, 5093 (1994).
- ³²S. Jang and G. A. Voth, *The Journal of Chemical Physics* **111**, 2371 (1999).
- ³³I. R. Craig and D. E. Manolopoulos, *The Journal of Chemical Physics* **121**, 3368 (2004).
- ³⁴B. J. Braams and D. E. Manolopoulos, *The Journal of chemical physics* **125** (2006).
- ³⁵S. Habershon, D. E. Manolopoulos, T. E. Markland, and T. F. Miller, *Annual Review of Physical Chemistry* **64**, 387 (2013).
- ³⁶M. Rossi, M. Ceriotti, and D. E. Manolopoulos, *The Journal of Chemical Physics* **140**, 234116 (2014).
- ³⁷M. Rossi, V. Kapil, and M. Ceriotti, *The Journal of Chemical Physics* **148**, 102301 (2017).
- ³⁸S. Althorpe, *The European Physical Journal B* **94** (2021), 10.1140/epjb/s10051-021-00155-2.
- ³⁹M. J. Willatt, *Matsubara Dynamics and its Practical Implementation*, Ph.D. thesis (2017).
- ⁴⁰S. Habershon, G. S. Fanourgakis, and D. E. Manolopoulos, *The Journal of Chemical Physics* **129**, 074501 (2008).
- ⁴¹M. Rossi, H. Liu, F. Paesani, J. Bowman, and M. Ceriotti, *The Journal of Chemical Physics* **141**, 181101 (2014).
- ⁴²G. R. Medders and F. Paesani, *Journal of Chemical Theory and Computation* **11**, 1145 (2015).
- ⁴³D. R. Moberg, S. C. Straight, C. Knight, and F. Paesani, *The Journal of Physical Chemistry Letters* **8**, 2579 (2017).
- ⁴⁴S. K. Reddy, D. R. Moberg, S. C. Straight, and F. Paesani, *The Journal of Chemical Physics* **147**, 244504 (2017).
- ⁴⁵K. Druzicki, M. Krzystyniak, D. Hollas, V. Kapil, P. Slavicek, G. Romanelli, and F. Fernandez-Alonso, *Journal of Physics: Conference Series* **1055**, 012003 (2018).
- ⁴⁶T. Markland and M. Ceriotti, *Nature Reviews Chemistry* **2**, 0109 (2018).
- ⁴⁷K. M. Hunter, F. A. Shakib, and F. Paesani, *The Journal of Physical Chemistry B* **122**, 10754 (2018).
- ⁴⁸Z. Tong, P. E. Videla, K. A. Jung, V. S. Batista, and X. Sun, *The Journal of Chemical Physics* **153**, 034117 (2020).
- ⁴⁹V. S. S. Inakollu and H.-B. Yu, *Structural Dynamics* **8** (2021).
- ⁵⁰T. E. Li, A. Nitzan, S. Hammes-Schiffer, and J. E. Subotnik, *The journal of physical chemistry letters*, 3890 (2022).
- ⁵¹A. Z. Lieberherr, S. T. E. Furniss, J. E. Lawrence, and D. E. Manolopoulos, *The Journal of chemical physics* **158** **23** (2023).
- ⁵²T. Khuu, T. Schleif, A. Mohamed, S. Mitra, M. A. Johnson, J. Valdiviezo, J. P. Heindel, and T. Head-Gordon, *The Journal of Physical Chemistry A* **127**, 7501 (2023).
- ⁵³J. Bowles, D. Laage, J. D. L. F. Diez, J. Richardi, R. Vuilleumier, and R. Spezia (2024).
- ⁵⁴R. Beckmann, C. Schran, F. Briec, and D. Marx, *Phys. Chem. Chem. Phys.* **26**, 22846 (2024).
- ⁵⁵A. Gomez, W. Thompson, and D. Laage, *Nature chemistry* (2024).
- ⁵⁶A. Nandi, R. Conte, P. Pandey, P. L. Houston, C. Qu, Q. Yu, and J. M. Bowman, *Journal of Chemical Theory and Computation* **21**, 5208 (2025).
- ⁵⁷L. T. S. de Miranda, M. S. Gomes-Filho, M. Rossi, L. S. Pedroza, and A. R. Rocha (2025).
- ⁵⁸A. Rana, P. A. Harville, T. Khuu, R. A. LaCour, T. Head-Gordon, and M. A. Johnson, *The Journal of Physical Chemistry Letters* **16**, 5252 (2025).
- ⁵⁹G. Trenins, M. J. Willatt, and S. C. Althorpe, *The Journal of Chemical Physics* **151**, 054109 (2019).
- ⁶⁰A. Witt, S. D. Ivanov, M. Shiga, H. Forbert, and D. Marx, *The Journal of Chemical Physics* **130**, 194510 (2009).
- ⁶¹S. D. Ivanov, A. Witt, M. Shiga, and D. Marx, *The Journal of Chemical Physics* **132**, 031101 (2010).
- ⁶²T. Fletcher, A. Zhu, J. E. Lawrence, and D. E. Manolopoulos, *The Journal of Chemical Physics* **155**, 231101 (2021).
- ⁶³C. Haggard, V. G. Sadhasivam, G. Trenins, and S. C. Althorpe, *The Journal of Chemical Physics* **155**, 174120 (2021).
- ⁶⁴F. Musil, I. Zaporozhets, F. Noé, C. Clementi, and V. Kapil, *The Journal of Chemical Physics* **157**, 181102 (2022).
- ⁶⁵I. Zaporozhets, F. Musil, V. Kapil, and C. Clementi, *The Journal of Chemical Physics* **161**, 134102 (2024).
- ⁶⁶T. D. Hone, P. J. Rossky, and G. A. Voth, *The Journal of Chemical Physics* **124**, 154103 (2006).
- ⁶⁷M. Ceriotti, M. Parrinello, T. E. Markland, and D. E. Manolopoulos, *The Journal of Chemical Physics* **133**, 124104 (2010).
- ⁶⁸J. Cao and G. A. Voth, *The Journal of Chemical Physics* **100**, 5106 (1994).
- ⁶⁹G. Trenins and S. C. Althorpe, *The Journal of Chemical Physics* **149**, 014102 (2018).
- ⁷⁰P. Ravindra, X. Advincula, C. Schran, A. Michaelides, and V. Kapil, *Nature Communications* **15** (2024), 10.1038/s41467-024-51124-z.
- ⁷¹P. Ravindra, X. R. Advincula, B. X. Shi, S. W. Coles, A. Michaelides, and V. Kapil (2024).
- ⁷²R. Rashmi, T. O. Balogun, G. Azom, H. Agnew, R. Kumar, and F. Paesani, *ACS Nano* **19**, 4876 (2025).
- ⁷³I. Zaporozhets, F. Musil, V. Kapil, and C. Clementi, *The Journal of chemical physics* **161** **13** (2024).
- ⁷⁴G. Bussi, D. Donadio, and M. Parrinello, *The Journal of Chemical Physics* **126**, 014101 (2007).
- ⁷⁵Y. Litman, V. Kapil, Y. M. Y. Feldman, D. Tisi, T. Begušić, K. Fidanyan, G. Fraux, J. Higer, M. Kellner, T. E. Li, E. S. Pós, E. Stocco, G. Trenins, B. Hirshberg, M. Rossi, and M. Ceriotti, *The Journal of Chemical Physics* **161**, 062504 (2024).
- ⁷⁶H. Partridge and D. W. Schwenke, *The Journal of Chemical Physics* **106**, 4618 (1997).
- ⁷⁷I. Batatia, D. P. Kovacs, G. N. C. Simm, C. Ortner, and G. Csányi, in *Advances in Neural Information Processing Systems*, edited by A. H. Oh, A. Agarwal, D. Belgrave, and K. Cho (2022).
- ⁷⁸I. Batatia, S. Batzner, D. P. Kovács, A. Musaelian, G. N. C. Simm, R. Drautz, C. Ortner, B. Kozinsky, and G. Csányi, “The design space of e(3)-equivariant atom-centered interatomic potentials,” (2022), arXiv:2205.06643.
- ⁷⁹A. D. Becke, *The Journal of Chemical Physics* **98**, 5648 (1993).
- ⁸⁰P. J. Stephens, F. J. Devlin, C. F. Chabalowski, and M. J. Frisch, *The Journal of Physical Chemistry* **98**, 11623 (1994).
- ⁸¹A. Tkatchenko and M. Scheffler, *Phys. Rev. Lett.* **102**, 073005 (2009).
- ⁸²J. Heyd, G. E. Scuseria, and M. Ernzerhof, *The Journal of Chemical Physics* **118**, 8207 (2003).
- ⁸³A. V. Krukau, O. A. Vydrov, A. F. Izmaylov, and G. E. Scuseria, *The Journal of Chemical Physics* **125**, 224106 (2006).
- ⁸⁴A. Tkatchenko, R. A. DiStasio, R. Car, and M. Scheffler, *Physical Review Letters* **108**, 236402 (2012).
- ⁸⁵Y. Rubner, C. Tomasi, and L. Guibas, in *Sixth International Conference on Computer Vision (IEEE Cat. No.98CH36271)* (1998) pp. 59–66.
- ⁸⁶D. A. Thomas, E. Mucha, M. Lettow, G. Meijer, M. Rossi, and G. von Helden, *Journal of the American Chemical Society* **141**, 5815 (2019).
- ⁸⁷F. Brivio, J. M. Frost, J. M. Skelton, A. J. Jackson, O. J. Weber, M. T. Weller, A. R. Goñi, A. M. A. Leguy, P. R. F. Barnes, and A. Walsh, *Physical Review B* **92**, 144308 (2015).

- ⁸⁸J. Lahnsteiner, G. Kresse, J. Heinen, and M. Bokdam, *Physical Review Materials* **2**, 073604 (2018), 1804.08253.
- ⁸⁹J. Li, M. Bouchard, P. Reiss, D. Aldakov, S. Pouget, R. Demadrille, C. Aumaitre, B. Frick, D. Djurado, M. Rossi, and P. Rinke, *The Journal of Physical Chemistry Letters* **9**, 3969 (2018).
- ⁹⁰A. Gold-Parker, P. M. Gehring, J. M. Skelton, I. C. Smith, D. Parshall, J. M. Frost, H. I. Karunadasa, A. Walsh, and M. F. Toney, *Proceedings of the National Academy of Sciences* **115**, 11905 (2018).
- ⁹¹T. Liu, S.-Y. Yue, S. Ratnasingham, T. Degousée, P. Varsini, J. Briscoe, M. A. McLachlan, M. Hu, and O. Fenwick, *ACS Applied Materials & Interfaces* **11**, 47507 (2019).
- ⁹²A. Giri, *Nanoscale* **13**, 685 (2021).
- ⁹³G. Schuck, D. M. Többsen, M. Koch-Müller, I. Efthimiopoulos, and S. Schorr, *The Journal of Physical Chemistry C* **122**, 5227 (2018).
- ⁹⁴V. Kapil, D. P. Kovács, G. Csányi, and A. Michaelides, *Faraday Discuss.* **249**, 50 (2024).
- ⁹⁵M. T. Weller, O. J. Weber, P. F. Henry, A. M. Di Pumpo, and T. C. Hansen, *Chemical Communications* **51**, 4180 (2015).
- ⁹⁶M. Rossi, P. Gasparotto, and M. Ceriotti, *Physical Review Letters* **117**, 115702 (2016).
- ⁹⁷M. A. Morales, J. M. McMahon, C. Pierleoni, and D. M. Ceperley, *Physical Review Letters* **110**, 065702 (2013).
- ⁹⁸E. Balog, A. L. Hughes, and G. J. Martyna, *The Journal of Chemical Physics* **112**, 870 (2000).
- ⁹⁹L. Wang, C. Isborn, and T. Markland, in *Computational Approaches for Studying Enzyme Mechanism Part A*, *Methods in Enzymology*, Vol. 577, edited by G. A. Voth (Academic Press, 2016) pp. 389–418.
- ¹⁰⁰J. P. Klinman and A. Kohen, *Annual Review of Biochemistry* **82**, 471 (2013).
- ¹⁰¹F. Angiolari, S. Huppert, F. Pietrucci, and R. Spezia, *The Journal of Physical Chemistry Letters* **14**, 5102 (2023).
- ¹⁰²F. Uhl, D. Marx, and M. Ceriotti, *The Journal of Chemical Physics* **145**, 054101 (2016).
- ¹⁰³J. Lill, G. Parker, and J. Light, *Chemical Physics Letters* **89**, 483 (1982).
- ¹⁰⁴J. Cao and G. A. Voth, *The Journal of Chemical Physics* **101**, 6168 (1994).
- ¹⁰⁵X. Sun and W. H. Miller, *The Journal of Chemical Physics* **110**, 6635 (1999).
- ¹⁰⁶Y. Wang and J. M. Bowman, *The Journal of Chemical Physics* **134**, 154510 (2011).
- ¹⁰⁷Y. Wang and J. M. Bowman, *The Journal of Chemical Physics* **136**, 144113 (2012).
- ¹⁰⁸D. Marx, M. E. Tuckerman, and G. J. Martyna, *Computer Physics Communications* **118**, 166 (1999).
- ¹⁰⁹D. Marx and M. Parrinello, *The Journal of Chemical Physics* **104**, 4077 (1996).
- ¹¹⁰M. E. Tuckerman, D. Marx, M. L. Klein, and M. Parrinello, *The Journal of Chemical Physics* **104**, 5579 (1996).
- ¹¹¹G. Bussi and M. Parrinello, *Computer Physics Communications* **179**, 26 (2008), special issue based on the Conference on Computational Physics 2007.
- ¹¹²D. P. Kovács, J. H. Moore, N. J. Browning, I. Batatia, J. T. Horton, V. Kapil, W. C. Witt, I.-B. Magdáu, D. J. Cole, and G. Csányi, “Maceoff23: Transferable machine learning force fields for organic molecules,” (2023), arXiv:2312.15211 [physics.chem-ph].
- ¹¹³S. Kokott, F. Merz, Y. Yao, C. Carbogno, M. Rossi, V. Havu, M. Rampp, M. Scheffler, and V. Blum, *The Journal of Chemical Physics* **161**, 024112 (2024).
- ¹¹⁴J. Heyd, G. E. Scuseria, and M. Ernzerhof, *The Journal of Chemical Physics* **124**, 219906 (2006).
- ¹¹⁵J. P. Perdew, K. Burke, and M. Ernzerhof, *Physical Review Letters* **78**, 1396 (1997).
- ¹¹⁶J. P. Perdew, K. Burke, and M. Ernzerhof, *Physical Review Letters* **77**, 3865 (1996).
- ¹¹⁷S. C. Althorpe, *Annual Review of Physical Chemistry* **75**, 397 (2024).
- ¹¹⁸G. Bussi, T. Zykova-Timan, and M. Parrinello, *The Journal of Chemical Physics* **130**, 074101 (2009).
- ¹¹⁹L. Martínez, R. Andrade, E. Birgin, and J. M. Martínez, *Journal of Computational Chemistry* **30**, 2157 (2009).
- ¹²⁰S. Habershon, T. E. Markland, and D. E. Manolopoulos, *The Journal of Chemical Physics* **131**, 024501 (2009).
- ¹²¹F. L. Thiemann, N. O’Neill, V. Kapil, A. Michaelides, and C. Schran, *Journal of Physics: Condensed Matter* **37**, 073002 (2024).
- ¹²²G. T. Gipson, K. S. Tatsuoka, B. C. Sweatman, and S. C. Connor, *Journal of Magnetic Resonance* **183**, 269 (2006).
- ¹²³D. M. Haaland, R. G. Easterling, and D. A. Vopicka, *Applied Spectroscopy* **39**, 73 (1985).
- ¹²⁴Y. S. Chang and J. H. Shaw, *Applied Spectroscopy* **31**, 213 (1977).
- ¹²⁵J. Johns, *Journal of Molecular Spectroscopy* **125**, 442 (1987).
- ¹²⁶D. Benner, C. P. Rinsland, V. Devi, M. A. H. Smith, and D. Atkins, *Journal of Quantitative Spectroscopy and Radiative Transfer* **53**, 705 (1995).
- ¹²⁷P. Bevington and D. Robinson, *Data Reduction and Error Analysis for the Physical Sciences* (McGraw-Hill Education, 2003).
- ¹²⁸T. Okada, K. Komatsu, T. Kawamoto, T. Yamanaka, and H. Kagi, *Spectrochimica Acta Part A: Molecular and Biomolecular Spectroscopy* **61**, 2423 (2005), georaman 2004: Sixth International Conference on Raman Spectroscopy Applied to the Earth and Planetary Sciences.
- ¹²⁹A. A. Bakulin, O. Selig, H. J. Bakker, Y. L. Rezus, C. Müller, T. Glaser, R. Lovrincic, Z. Sun, Z. Chen, A. Walsh, J. M. Frost, and T. L. C. Jansen, *The Journal of Physical Chemistry Letters* **6**, 3663 (2015).
- ¹³⁰R. Wasylishen, O. Knop, and J. Macdonald, *Solid State Communications* **56**, 581 (1985).
- ¹³¹T. Baikie, Y. Fang, J. M. Kadro, M. Schreyer, F. Wei, S. G. Mhaisalkar, M. Graetzl, and T. J. White, *Journal of Materials Chemistry A* **1**, 5628 (2013).
- ¹³²P. Virtanen, R. Gommers, T. E. Oliphant, M. Haberland, T. Reddy, D. Cournapeau, E. Burovski, P. Peterson, W. Weckesser, J. Bright, S. J. van der Walt, M. Brett, J. Wilson, K. J. Millman, N. Mayorov, A. R. J. Nelson, E. Jones, R. Kern, E. Larson, C. J. Carey, . Polat, Y. Feng, E. W. Moore, S. Vandeplas, D. Laxalde, J. Perktold, R. Cimrman, I. Henriksen, E. A. Quintero, C. R. Harris, A. M. Archibald, A. Ribeiro, F. Pedregosa, P. van Mulbregt, *et al.*, *Nature Methods* **17**, 261 (2020).
- ¹³³V. Kapil, C. Schran, A. Zen, J. Chen, C. J. Pickard, and A. Michaelides, *Nature* **609**, 512–516 (2022).
- ¹³⁴S. Jang and G. A. Voth, *The Journal of Chemical Physics* **111**, 2357 (1999).
- ¹³⁵J. Cao and G. A. Voth, *The Journal of Chemical Physics* **99**, 10070 (1993).
- ¹³⁶J. O. Richardson and S. C. Althorpe, *The Journal of Chemical Physics* **131**, 214106 (2009).
- ¹³⁷H. Wang, X. Sun, and W. H. Miller, *The Journal of Chemical Physics* **108**, 9726 (1998).
- ¹³⁸J. Liu and W. H. Miller, *The Journal of Chemical Physics* **134**, 104101 (2011).
- ¹³⁹H. Wang, M. Thoss, and W. H. Miller, *The Journal of Chemical Physics* **112**, 47 (2000).
- ¹⁴⁰T. D. Loose, P. G. Sahrman, and G. A. Voth, *Journal of Chemical Theory and Computation* **18**, 5856 (2022).
- ¹⁴¹O. Christiansen, *Phys. Chem. Chem. Phys.* **14**, 6672 (2012).
- ¹⁴²N. Makri, *Journal of Mathematical Physics* **36**, 2430 (1995).
- ¹⁴³D. E. Makarov and N. Makri, *Chemical Physics Letters* **221**, 482 (1994).
- ¹⁴⁴N. Makri and D. E. Makarov, *The Journal of Chemical Physics* **102**, 4600 (1995).
- ¹⁴⁵N. Makri and D. E. Makarov, *The Journal of Chemical Physics* **102**, 4611 (1995).
- ¹⁴⁶N. Makri, *The Journal of Physical Chemistry A* **102**, 4414 (1998).
- ¹⁴⁷T. Begusic, X. Tao, G. A. Blake, and T. F. Miller, *The Journal of chemical physics* **156**, 131102 (2022).
- ¹⁴⁸M. Shiga and A. Nakayama, *Chemical Physics Letters* **451**, 175 (2008).
- ¹⁴⁹F. Calvo, P. Parneix, and N.-T. Van-Oanh, *The Journal of Chemical Physics* **132**, 124308 (2010).
- ¹⁵⁰R.-H. Zheng, W.-Z. Guan, S.-C. Zhang, and W.-M. Wei, *The Journal of Physical Chemistry C* **128**, 18082 (2024).
- ¹⁵¹Richard J. Gowers, Max Linke, Jonathan Barnoud, Tyler J. E. Reddy, Manuel N. Melo, Sean L. Seyler, Jan Domański, David L. Dotson, Sébastien Buchoux, Ian M. Kenney, and Oliver Beckstein, in *Proceedings of the 15th Python in Science Conference*, edited by Sebastian Benthall and Scott Rostrup (2016) pp. 98 – 105.
- ¹⁵²N. Michaud-Agrawal, E. J. Denning, T. B. Woolf, and O. Beckstein, *Journal of Computational Chemistry* **32**, 2319 (2011).
- ¹⁵³M. Ceriotti, V. Kapil, P. Gasparotto, and D. Hollas, “Gle4md: Generalized langevin equation thermostat repository,” <http://gle4md.org/>, accessed: August 21, 2025.

¹⁵⁴F. Harris, Proceedings of the IEEE **66**, 51 (1978).

Supplementary Information for “Vibrational Spectra of Materials and Molecules from Partially-Adiabatic Elevated-Temperature Centroid Molecular Dynamics”

Jorge Castro,¹ George Trenins,¹ Venkat Kapil,^{2,3} and Mariana Rossi^{1, a)}

¹⁾*MPI for the Structure and Dynamics of Matter, Hamburg,
Germany*

²⁾*Department of Physics and Astronomy, University College London, 7-19 Gordon St,
London WC1H 0AH, UK*

³⁾*Thomas Young Centre and London Centre for Nanotechnology, 9 Gordon St,
London WC1H 0AH*

(Dated: 25 August 2025)

^{a)}Electronic mail: mariana.rossi@mpsd.mpg.de

CONTENTS

S1. Curvature problem in water monomer IR spectra	3
S2. CMD Mean-Field Forces and Critical Radius r_x	5
S3. Elevated temperature tests	6
S3.1. Water monomer	6
S3.2. CAF	7
S3.3. MAPI	8
S4. Computational Details for PA-T_e-CMD Benchmarking	9
S4.1. Water Molecule	9
S4.2. Methylammonium Lead Iodide	10
S4.3. Carbonic Acid Fluoride	10
S4.4. Liquid Water at Different Pressures	11
S5. Computational Details for Additional Molecular Simulation Methods	12
S5.1. Classical Molecular Dynamics (MD)	12
S5.2. Centroid Molecular Dynamics (CMD)	12
S5.3. Thermostatted Ring Polymer Molecular Dynamics (TRPMD)	13
S5.4. Ab Initio Molecular Dynamics (AIMD)	13
S6. Spectral Similarity Metric: Earth Mover’s Distance	14
S7. Additional Results: CAF	16
S7.1. Assessment of the MACE potential for CAF	16
S7.2. Effect of Elevated Temperatures on T_e -PIGS Infrared Spectra of CAF	17
S7.3. Free energy surfaces of CAF at 100K	17
S7.4. CAF equilibrium O–H and F–H bond lengths	18
S7.5. O-H bond length distribution of CAF with different methods	19
S8. Additional Results: MAPI	19
S8.1. Comparison of Anharmonic Potentials in Methylammonium Lead Iodide (Orthorhombic Phase at 110 K vs Tetragonal Phase at 300 K)	19

S9. Path-Integral Simulations of High-Pressure Liquid Water: Resolving Subtle Vibrational Shifts	21
S10. Additional Tables	25
S10.1. VDOS frequencies of CAF at 100K	25
S10.2. VDOS frequencies of MAPI at 300K	25
S10.3. VDOS frequencies of MAPI at 110K	26
S10.4. Fitting of liquid water VDOS spectra	26
References	27

S1. CURVATURE PROBLEM IN WATER MONOMER IR SPECTRA

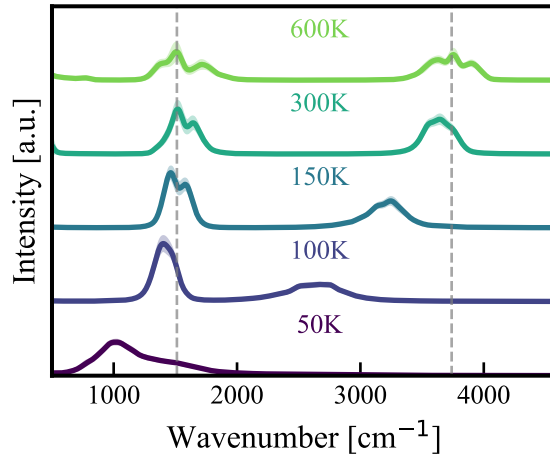


FIG. S1. The curvature problem in IR water monomer spectra. This artifact causes a red shift in vibrational frequencies as the temperature decreases, particularly in the O–H bond stretching band, with a smaller effect on the bending vibrational band. The dashed line represents the exact result.

To demonstrate that the red shift of the O–H stretching vibrational band in the CMD simulation of the water monomer at 50 K, caused by the curvature problem, leads to its merging with the bending vibrational mode, we projected the IR spectrum onto harmonic normal modes and selected those corresponding to the bending and O–H stretching motions (see Fig. S2). The results confirm that the three IR-active vibrational modes indeed merge into a broad feature in the CMD IR spectrum. In particular, the O–H stretching bands exhibit a shift that exceeds 2000 cm^{-1} , highlighting the severity of the curvature problem in the calculation of the vibrational spectra.

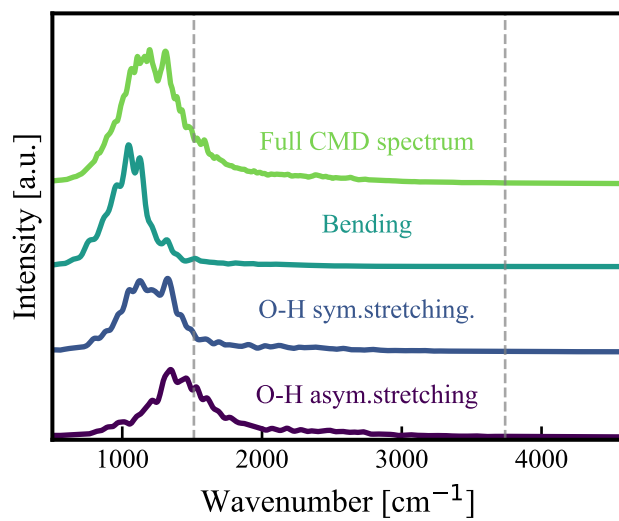


FIG. S2. Normal-mode projection of the vibrational spectrum of the water monomer computed using CMD at 50 K

S2. CMD MEAN-FIELD FORCES AND CRITICAL RADIUS r_x

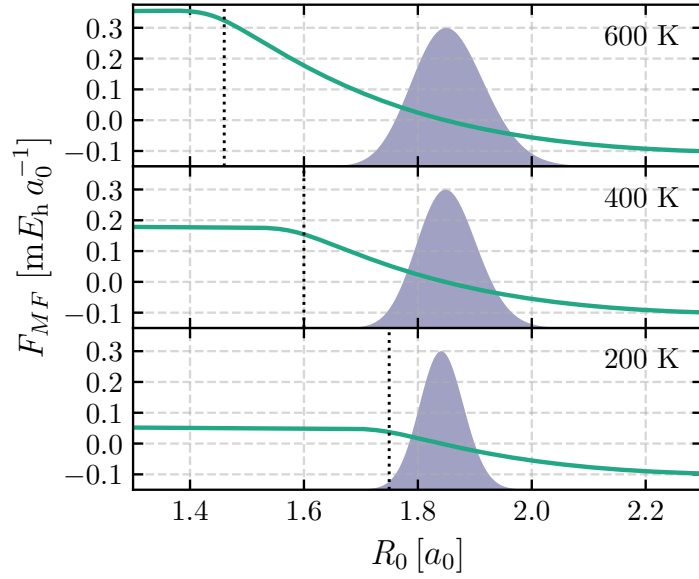


FIG. S3. The CMD mean-field force (green line) is shown together with the corresponding Boltzmann distribution (shaded purple). The dotted vertical lines mark the critical radius r_x , defined in Eq. (10) of the main text. Notably, r_x coincides with the onset of the force flattening, and the Boltzmann distribution overlaps with r_x at 200 K¹.

S3. ELEVATED TEMPERATURE TESTS

S3.1. Water monomer

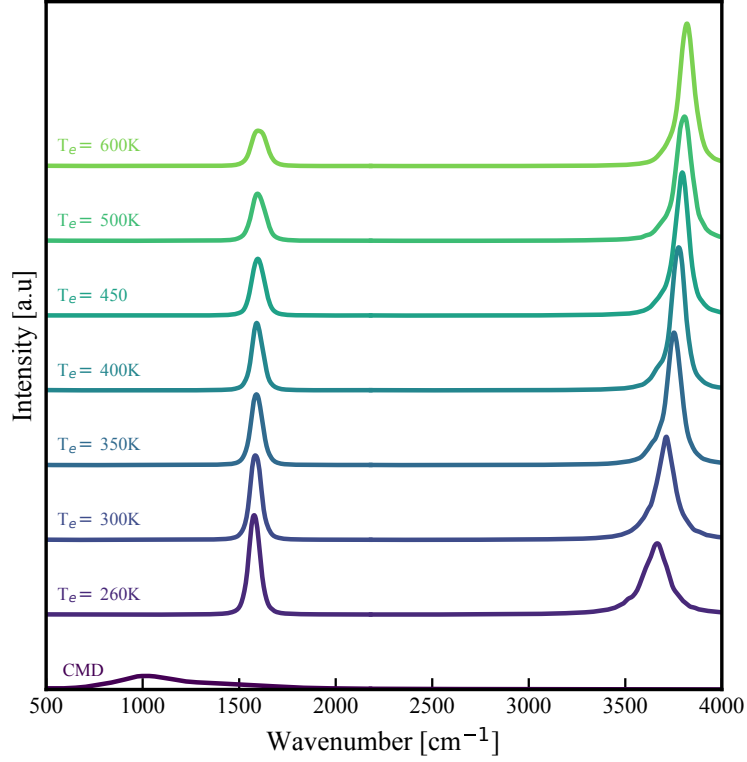


FIG. S4. Infrared spectra of the water monomer at 100 K computed using CMD and PA- T_e -CMD at various elevated temperatures T_e , with fixed thermostat parameters $\tau = 100$ fs and $\lambda = 0.01$ (referred to as Set C in the main text). CMD corresponds to the limiting case $T_e = T = 100$ K. As T_e is lowered, the excessive intensity in the O–H stretching band caused by kinetic energy leakage is reduced. However, overly low values of T_e reintroduce the curvature problem, highlighting the trade-off between suppressing leakage and avoiding spurious red shifts.

S3.2. CAF

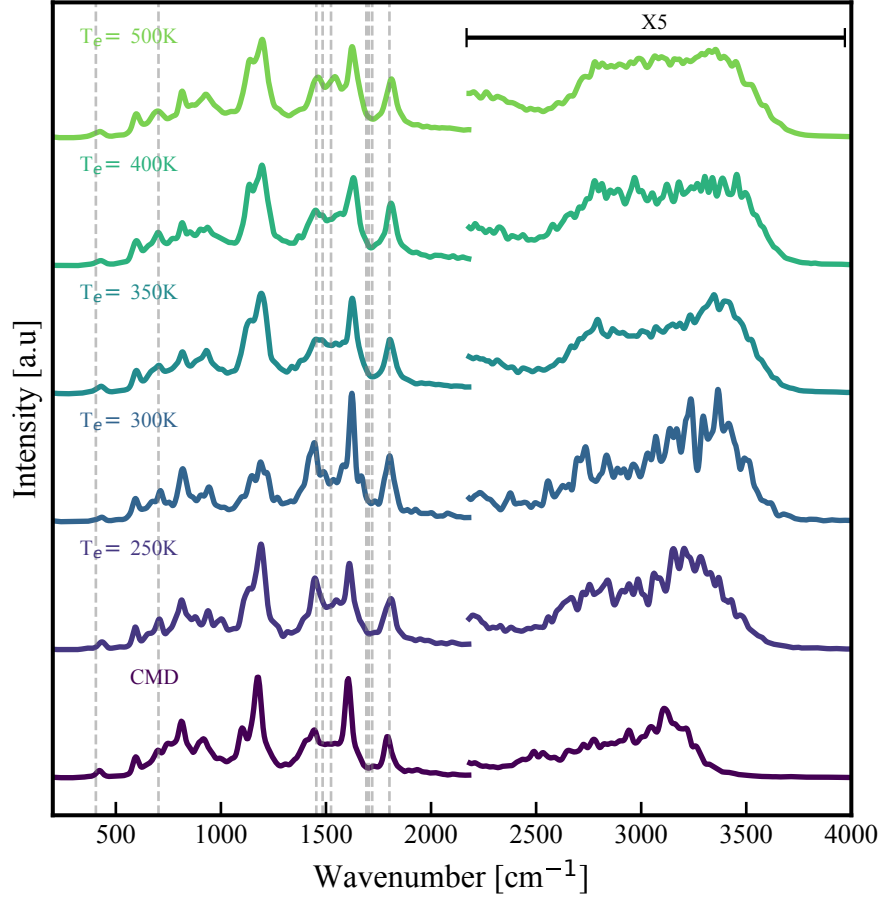


FIG. S5. Infrared spectra of carbonic acid fluoride (CAF) at 100 K computed using CMD and PA- T_e -CMD with increasing elevated temperatures T_e (thermostat parameters fixed to Set C: $\tau = 100$ fs, $\lambda = 0.01$). In standard CMD ($T_e = T = 100$ K), the O-H stretching modes are significantly broadened and red-shifted due to the curvature problem. These artifacts persist up to $T_e = 300$ K but disappear entirely at $T_e = 350$ K, indicating suppression of the curvature problem.

S3.3. MAPI

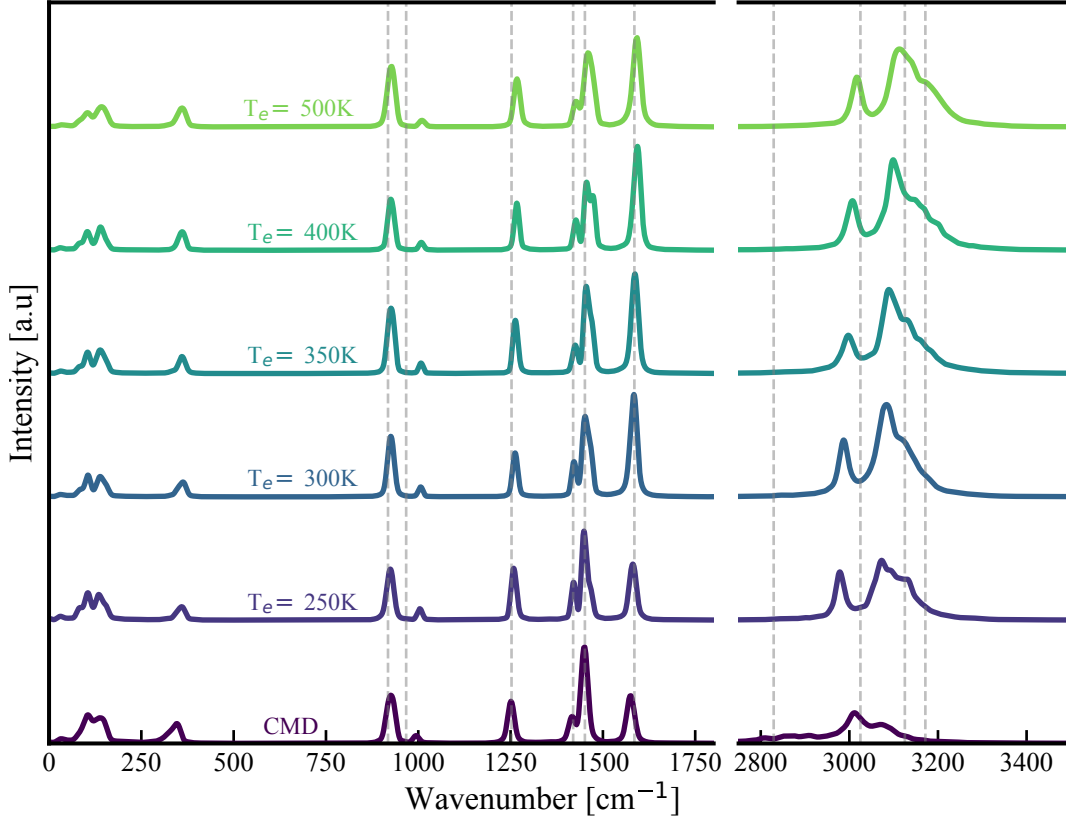


FIG. S6. Comparison of VDOS spectra of MAPI at 110 K, computed using CMD and thermostatted elevated-temperature methods at different values of the elevated temperature T_e . Two spectral regions are shown: the fingerprint region ($0\text{--}1800\text{ cm}^{-1}$) and the high-frequency stretching region ($2750\text{--}3500\text{ cm}^{-1}$). Vertical dashed lines mark selected experimental IR peak positions. N–H and C–H stretching features are strongly affected by the curvature problem in the CMD spectrum. As T_e increases, spurious red shifts and broadening are suppressed, and at $T_e = 350\text{ K}$, signatures of the curvature problem disappear. However, further increasing T_e promotes kinetic energy leakage from internal ring-polymer modes to the centroid, which degrades spectral resolution—particularly in the N–H stretching region.

S4. COMPUTATIONAL DETAILS FOR PA- T_e -CMD BENCHMARKING

While PA- T_e -CMD would be a consistent choice for generating thermalized starting configurations, in this study we employed path-integral molecular dynamics (PIMD) instead. As shown below, the results confirm that this choice does not affect the subsequent spectral analyses.

To validate this choice, we computed the IR spectra of a water monomer at three temperatures using PA- T_e -CMD for production, with initial configurations obtained from (i) PIMD with a standard PILE-L thermostat ($\tau = 10$ fs, $\lambda = 0.01$, time step = 0.25 fs) and (ii) PA- T_e -CMD thermalization using a two-temperature PILE-L thermostat with a time step of 0.01 fs ($\tau = 10$ fs, $\lambda = 0.01$, $\omega = 24000$ cm $^{-1}$). The results show no significant differences between the spectra obtained from these two thermalization procedures. This finding is important because PA- T_e -CMD thermalization is at least an order of magnitude more computationally expensive and substantially more time-consuming than PIMD. Consequently, these results support the use of PIMD as the preferred thermalization method for the more complex systems examined in the main paper. As shown in Fig. S7, the thermal sampling of the water monomer is not noticeably affected by the choice between PIMD and PA- T_e -CMD, further justifying our use of PIMD. Unless stated otherwise, spectral analyses used a lag time of 5000 fs, 15000 zero-padding steps, a Hanning window², and a sampling stride of 1 fs.

S4.1. Water Molecule

A single water molecule served as a benchmark for PA- T_e -CMD and T_e -PIGS at 600 K, 300 K, and 50 K. Simulations consisted of 100 ps thermalization followed by 100 independent 10 ps production runs.

For PA- T_e -CMD, we used the Partridge-Schwenke potential³ with 16 beads and $T_e = 600$ K, consistent with prior studies⁴⁻⁶. Thermalization was performed using a PILE-L thermostat ($\tau = 10$ ps) and a 0.5 fs time step. A 0.01 fs time step was used in production, and data were recorded every 0.5 fs. IR spectra were obtained via Fourier transforms of the dipole-dipole autocorrelation function, using a lag time of 1500 fs, 3000 zero-padding steps and sampling stride of 1 fs.

S4.2. Methylammonium Lead Iodide

We computed the vibrational density of states (VDOS) for MAPI at 110 K and 300 K using a $3 \times 3 \times 3$ supercell, with initial structures optimized to match neutron powder diffraction data⁷. Simulations employed a MACE potential^{8,9} trained on HSE06+vdW DFT data¹⁰⁻¹².

PIMD thermalization lasted 100 ps with a PILE-L thermostat ($\tau = 10$ fs) and a 0.25 fs time step. From these, 10 configurations were selected for PA- T_e -CMD. Production simulations ran for 10 ps using a 0.025 fs time step, $\omega = 24000$ cm⁻¹, $\tau = 20$ fs, $\lambda = 0.001$, and $T_e = 500$ K with 8 beads.

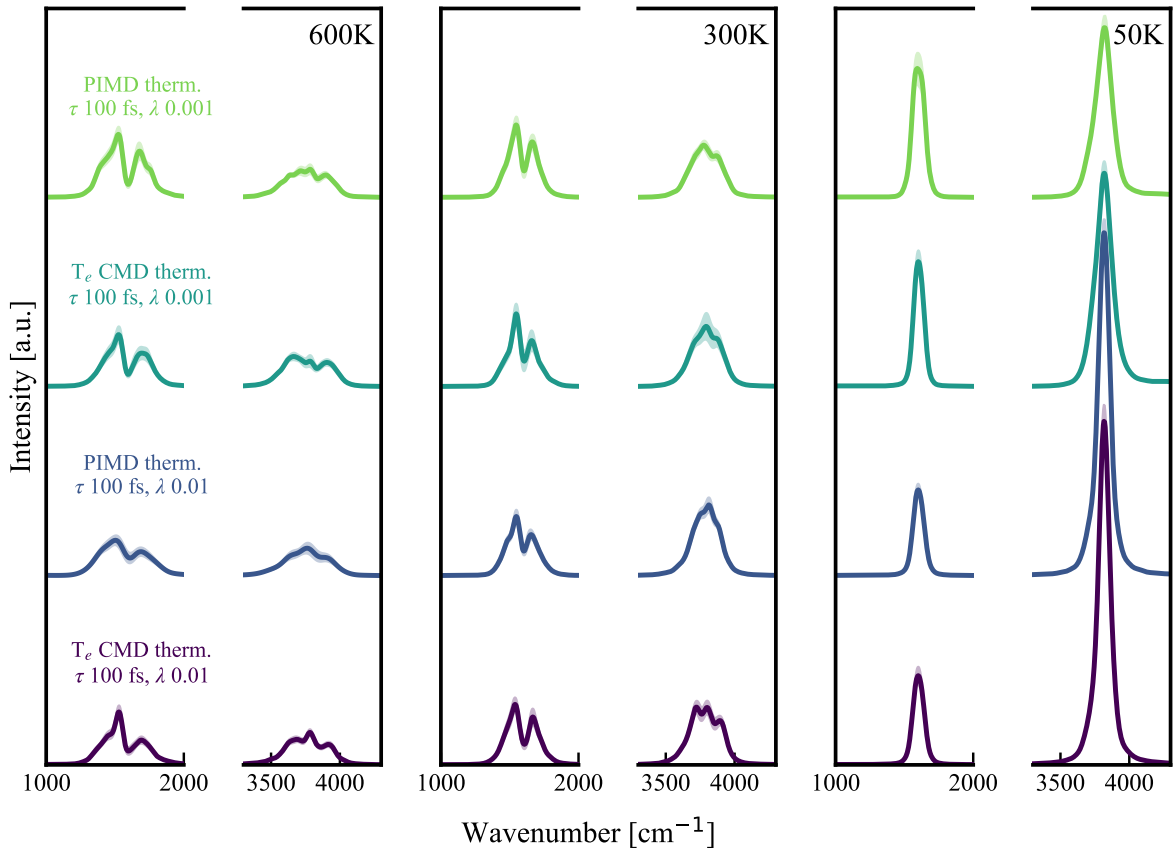


FIG. S7. IR spectra of water monomer computed using PA- T_e -CMD for production runs, from different thermalization methods: PIMD and PA- T_e -CMD

S4.3. Carbonic Acid Fluoride

We modeled CAF using a MACE potential trained on B3LYP+vdW^{13,14,15} DFT data. The training dataset contained 4000 structures sampled from AIMD (100 K, 200 K, 400 K) and TRPMD

(300 K).

PIMD thermalization was performed at 100 K for 200 ps with 64 beads, a PILE-L thermostat ($\tau = 10$ fs), and a 0.25 fs time step. From these, 50 configurations were selected for PA- T_e -CMD. Production runs lasted 10 fs using a 0.025 fs time step, with $\omega = 24000$ cm $^{-1}$, $\tau = 20$ fs, $\lambda = 0.001$, $T_e = 500$ K, and 8 beads.

S4.4. Liquid Water at Different Pressures

We computed the VDOS of liquid water at 300 K and pressures of 0.05 to 0.40 GPa. Initial configurations of 500 molecules were generated using PACKMOL¹⁶.

For each pressure, 2 ns PIMD equilibration in the NPT ensemble was conducted with 32 beads, an isotropic barostat¹⁷ ($\tau = 100$ fs), a Langevin thermostat ($\tau = 100$ fs), and a PILE-L thermostat ($\tau = 10$ fs). The average lattice parameters and densities obtained from classical MD and PIMD equilibrations are reported in Tables S1 and S2, respectively. Production simulations ran for 200 ps in NVT, followed by 200 independent PA- T_e -CMD runs of 10 fs each, with $\omega = 24000$ cm $^{-1}$, $\tau = 10$ fs, $\lambda = 0.001$, $T_e = 600$ K, and 32 beads, using the q-TIP4P/F¹⁸ water model.

Pressure [GPa]	Cell length [\AA]	ρ [g/cm 3]
0.05	24.49268	1.01697
0.40	23.66379	1.12594

TABLE S1. Equilibrated simulation cell dimensions and corresponding densities for liquid water at various pressures, obtained from 2 ns equilibration NPT classical MD simulations.

Pressure [GPa]	Cell length [\AA]	ρ [g/cm 3]
0.05	24.48006	1.01725
0.40	23.68406	1.12469

TABLE S2. Equilibrated simulation cell dimensions and corresponding densities for liquid water at various pressures, obtained from 2 ns equilibration NPT PIMD simulations.

S5. COMPUTATIONAL DETAILS FOR ADDITIONAL MOLECULAR SIMULATION METHODS

All simulations, except for the ab initio molecular dynamics (MD), used the same interatomic potentials as those employed in the PA-T_e-CMD simulations for the corresponding systems. For the water monomer, the Patridge-Schwanke (PS) water model³ was used, while liquid water simulations utilized the q-TIP4P/F model¹⁸. For MAPI, the MACE potential⁸ was employed, which was trained on DFT data using the HSE06 functional with many-body van der Waals (vdW) corrections^{10–12}. Similarly, the simulations for CAF relied on the MACE potential⁸, trained at the B3LYP+vdW functional level of theory¹². All simulations were performed using the i-PI code¹⁹.

S5.1. Classical Molecular Dynamics (MD)

Classical MD simulations were conducted by setting the number of replicas to one in i-PI. Simulations began with a 100 ps equilibration run in the NVT ensemble, using an SVR thermostat^{20,21} with a time constant of 10 fs. This was followed by a 100 ps sampling run in the same ensemble and with identical thermostat parameters. From the sampling trajectories, configurations were selected at 1 ps intervals to serve as starting points for 100 independent production simulations. Each production run lasted 10 ps and used an SVR thermostat with a relaxation time (τ) of 500 fs. For MAPI, only 50 independent production runs were performed, while 100 were used for CAF, and 200 for liquid water at different pressures. The IR and vibrational density of states (VDOS) spectra were computed using the same parameters as specified in the main text for PA-T_e-CMD and T_e-PIGS simulations.

S5.2. Centroid Molecular Dynamics (CMD)

Partially adiabatic CMD simulations were performed for the water monomer at all temperatures studied and for MAPI at 110 K. These simulations employed a PILE-G thermostat with a time constant of 20 fs and an adiabatic separation parameter of $\Omega = 24000 \text{ cm}^{-1}$. A timestep of 0.025 fs was used, and centroid positions were recorded every 1 fs. Simulations for the water monomer were run for 100 ps, with the number of replicas varying depending on the temperature: 16, 32, 64, 128, and 256 replicas for temperatures of 600 K, 300 K, 200 K, 100 K, and 50 K, respectively. For MAPI, simulations were conducted for 100 ps using 64 replicas at 110 K.

S5.3. Thermostatted Ring Polymer Molecular Dynamics (TRPMD)

TRPMD simulations were performed for the water monomer, liquid water, and CAF in the canonical ensemble. A PILE-G thermostat with a time constant of 500 fs and $\lambda = 0.5$ was used. The simulations employed a timestep of 0.25 fs, with bead positions recorded every 0.5 fs. Each system was subjected to 100 independent production runs, each lasting 10 ps. For the water monomer, simulations were performed at 50 K, 300 K, and 600 K using 256, 32, and 16 replicas, respectively. For liquid water, simulations at 300 K were conducted with 32 replicas, while for CAF, simulations at 100 K used 64 replicas. Additionally, for CAF we employed a generalized Langevin equation (GLE) thermostat²², using the GLE(C) parameterization. The corresponding A matrix was obtained from the official GLE repository²³

S5.4. Ab Initio Molecular Dynamics (AIMD)

AIMD simulations were conducted solely for CAF at 100 K. The i-PI code was used as the MD engine, while FHI-AIMS was used for force calculations based on density functional theory (DFT) at the B3LYP+vdW functional level of theory¹². Two independent equilibration runs were conducted in the NVT ensemble using an SVR thermostat with $\tau = 10$ fs. The final configurations from each equilibration run were used as starting points for two production simulations, each lasting 25 ps. A timestep of 1 fs was employed, with configurations recorded every 1 fs.

S6. SPECTRAL SIMILARITY METRIC: EARTH MOVER’S DISTANCE

To quantitatively evaluate the agreement between simulated and reference spectra, we employed the Earth Mover’s Distance (EMD)²⁴. EMD offers a physically intuitive measure of spectral dissimilarity, as it quantifies the minimum amount of “work” needed to transform one distribution into another—interpreting spectra as probability distributions of spectral weight. To validate the robustness of this metric in our context, we first benchmarked EMD using a controlled set of artificial spectra with known displacements and broadenings.

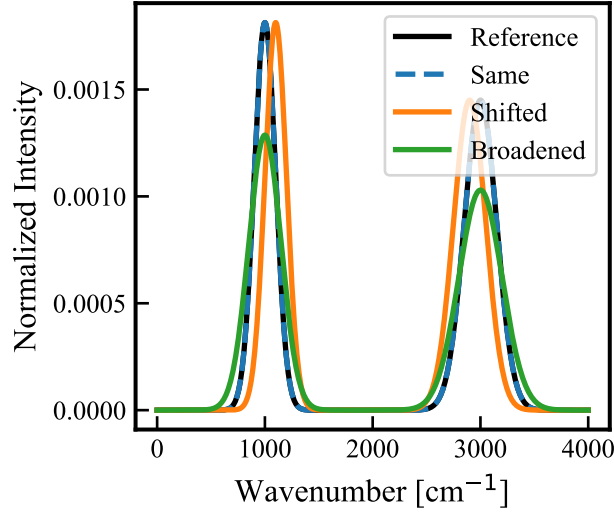


FIG. S8. Benchmark spectra used to validate the Earth Mover’s Distance (EMD) as a measure of spectral similarity. The reference spectrum (black) is compared to three test cases: an identical spectrum (blue), a version with shifted peaks (orange), and one with broadened features (green).

Spectrum	EMD index
Identical spectrum	0.00
Shifted peaks	100.00
Broadened peaks	81.26

TABLE S3. EMD values computed for the benchmark spectra shown in Figure S8. As expected, the identical spectrum yields zero distance, while peak shifts and broadenings increase the EMD in proportion to the spectral deformation.

The results of the EMD analysis applied to all methods and spectral regions discussed in the

main text for the water monomer are summarized in Table S6, where lower EMD values indicate closer agreement with the reference spectrum.

Parameter Set (τ [fs]/λ)	50 K	300 K	600 K	Total EMD Index
10/0.001 (Set B)	551.98	83.19	90.28	725.45
20/0.001 (Set E)	710.87	35.40	46.74	793.01
10/0.01 (Set A)	1128.06	269.43	55.07	1452.56
100/0.001 (Set D)	1329.36	216.29	97.64	1643.29
100/0.01 (Set C)	1830.37	275.07	93.22	2198.66

TABLE S4. Earth Mover’s Distance (EMD) between simulated and reference spectra for the water monomer at 50 K, 300 K, and 600 K using different values of τ and λ in PA- T_e -CMD. Lower values indicate better agreement.

S7. ADDITIONAL RESULTS: CAF

S7.1. Assessment of the MACE potential for CAF

To evaluate the fidelity of the machine-learned MACE potential for carbonic acid fluoride (CAF), we compared the VDOS spectrum obtained from classical MD simulations at 100 K using the MACE model with that from ab initio MD simulations at the same temperature. As shown in Fig. S9, the spectra are nearly indistinguishable, confirming that the potential accurately reproduces the structural and dynamical features encoded in the reference data. This validates the use of the MACE model for all subsequent quantum simulations of CAF presented in this work.

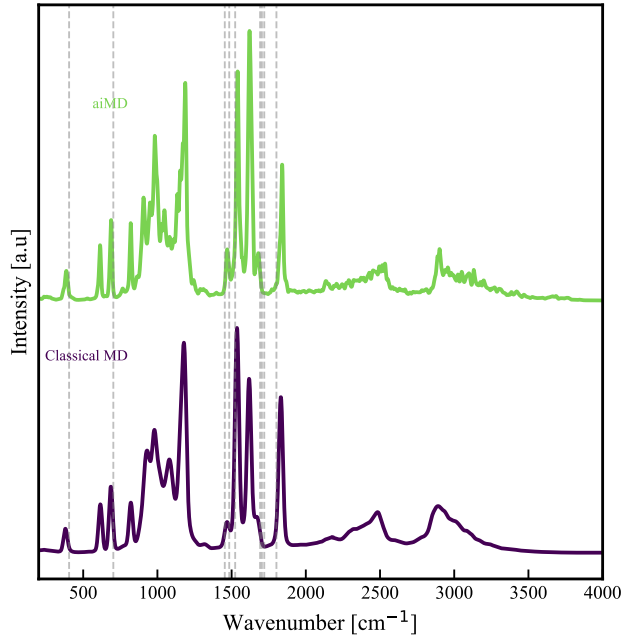


FIG. S9. Comparison between the vibrational density of states (VDOS) of carbonic acid fluoride (CAF) computed from ab initio molecular dynamics (AIMD) simulations at 100 K and classical molecular dynamics (MD) simulations using a MACE potential trained on the same AIMD data.

S7.2. Effect of Elevated Temperatures on T_e -PIGS Infrared Spectra of CAF

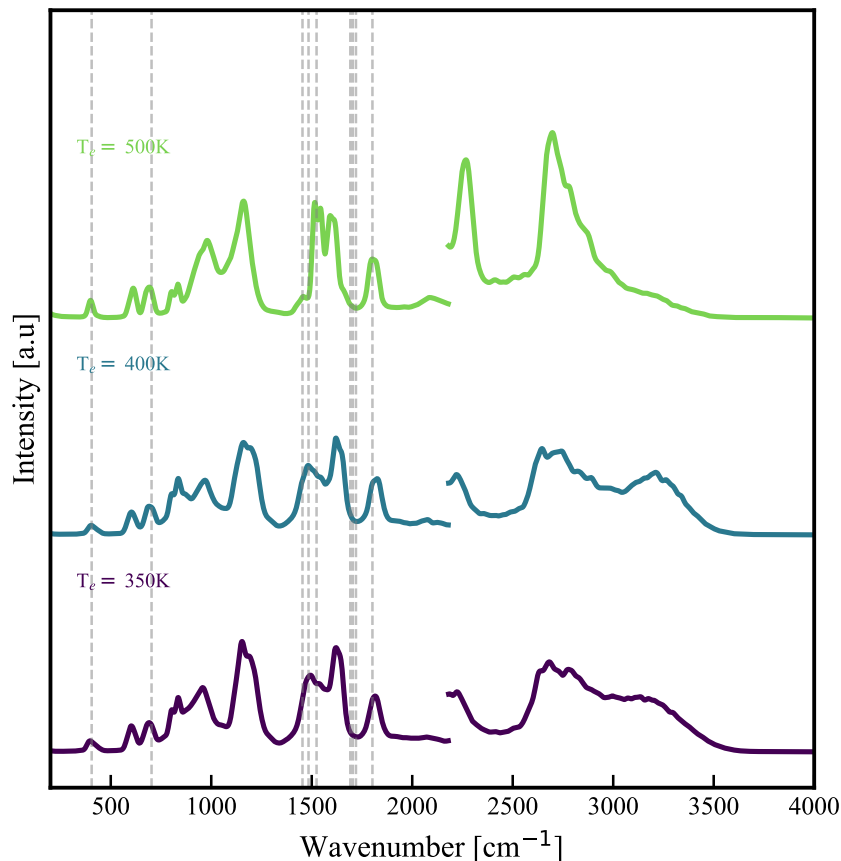


FIG. S10. Infrared spectra of carbonic acid fluoride (CAF) at 100 K computed using T_e -PIGS with increasing elevated temperatures T_e

S7.3. Free energy surfaces of CAF at 100K

To compute the free energy surfaces shown below, we extracted O–H and F–H bond distances from trajectory snapshots using MDAnalysis^{25,26}. For each hydrogen atom in a given frame, the nearest oxygen atom within a cutoff of 2.0 Å was identified and the corresponding O–H distance was recorded. The F–H distance was then computed as the distance between that same hydrogen and the only fluorine atom in the system. The equilibrium distances, identified as the minima of the free energy surfaces, are marked with white crosses and summarized in Table S5.

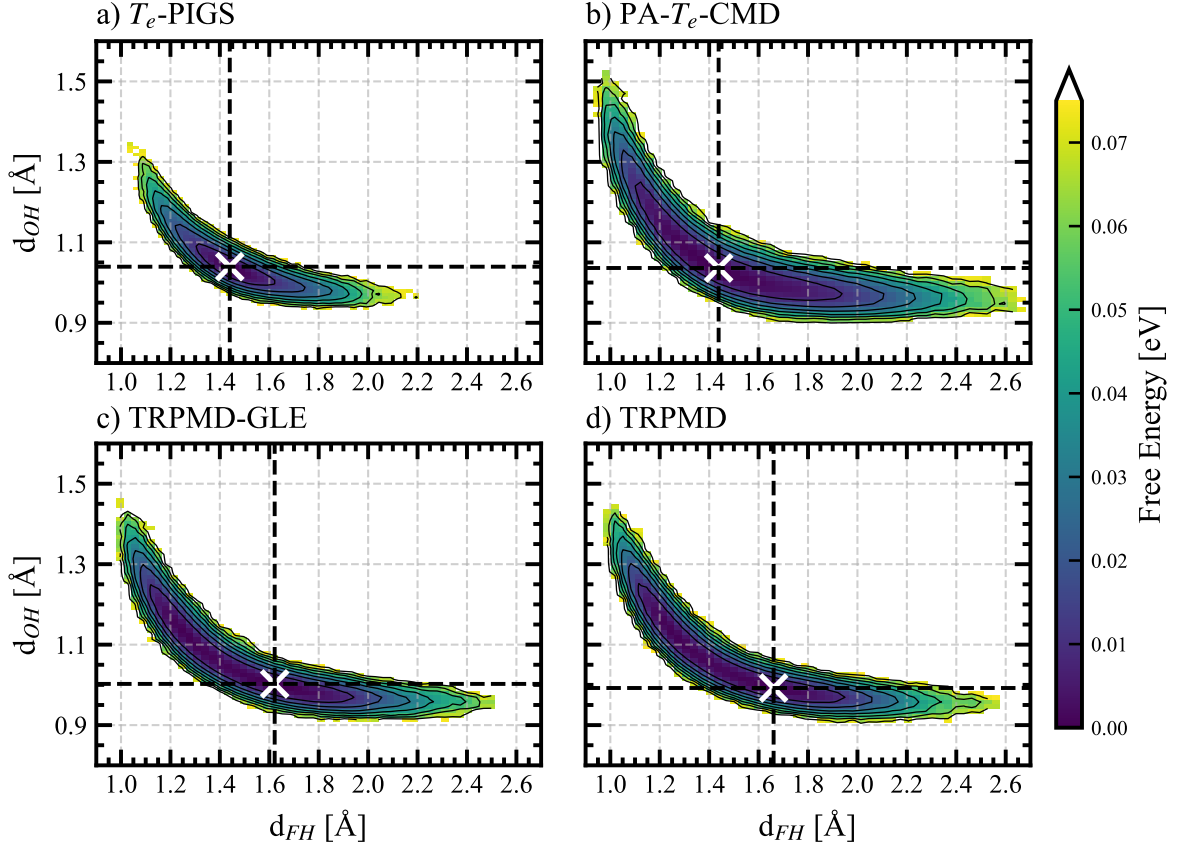


FIG. S11. Free energy surfaces derived from the joint probability density of the O–H and F–H distances. The free energy is calculated as $F = -k_B T \ln [P(d_{FH}, d_{OH})]$, where $P(d_{FH}, d_{OH})$ is the joint probability distribution of the F–H (d_{FH}) and O–H (d_{OH}) distances obtained from various PIMD simulation methods at $T = 100$ K. T_e -PIGS was simulated with the PMF trained at 500 K.

S7.4. CAF equilibrium O–H and F–H bond lengths

Method	d_{OH} [Å]	d_{FH} [Å]
T_e -PIGS	1.039	1.440
PA- T_e -CMD	1.036	1.438
TRPMD-GLE	1.002	1.622
TRPMD	0.992	1.661

TABLE S5. Equilibrium bond lengths and minimum free energy values from FES analysis.

S7.5. O-H bond length distribution of CAF with different methods

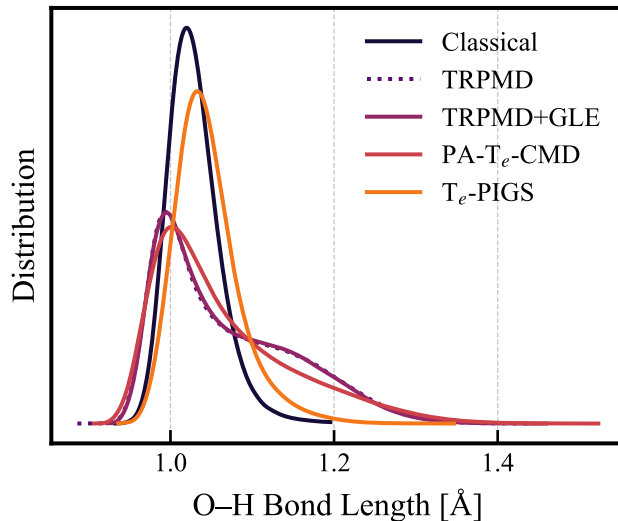


FIG. S12. Normalized O-H bond distributions for carbonic acid fluoride from five simulation methods.

S8. ADDITIONAL RESULTS: MAPI

S8.1. Comparison of Anharmonic Potentials in Methylammonium Lead Iodide (Orthorhombic Phase at 110 K vs Tetragonal Phase at 300 K)

We fitted the potential energy profiles of the two highest-frequency N-H stretching modes in MAPI, obtained from PA- T_e -CMD simulations, using a 5th-order polynomial model of the form

$$V(x) = ax^2 + bx^3 + cx^4 + dx^5,$$

where x is the displacement in Å, $V(x)$ is the potential energy in eV, and the coefficients a , b , c , and d have units chosen consistently (See table S6).

Phase	Mode	a (eV/Å ²)	b (eV/Å ³)	c (eV/Å ⁴)	d (eV/Å ⁵)
Orthorhombic (110 K)	Symmetric	21.29692	-62.73623	28.39502	165.88539
Orthorhombic (110 K)	Asymmetric	22.74816	-1.57264	41.84458	-0.28620
Tetragonal (300 K)	Symmetric	12.24795	-14.36068	9.91304	-4.83641
Tetragonal (300 K)	Asymmetric	15.44889	-0.99118	12.89128	-1.41118

TABLE S6. Polynomial fitting coefficients for the potential energy profiles of the symmetric and asymmetric N–H stretching modes in orthorhombic (110 K) and tetragonal (300 K) MAPI, obtained from PA-T_e-CMD simulations.

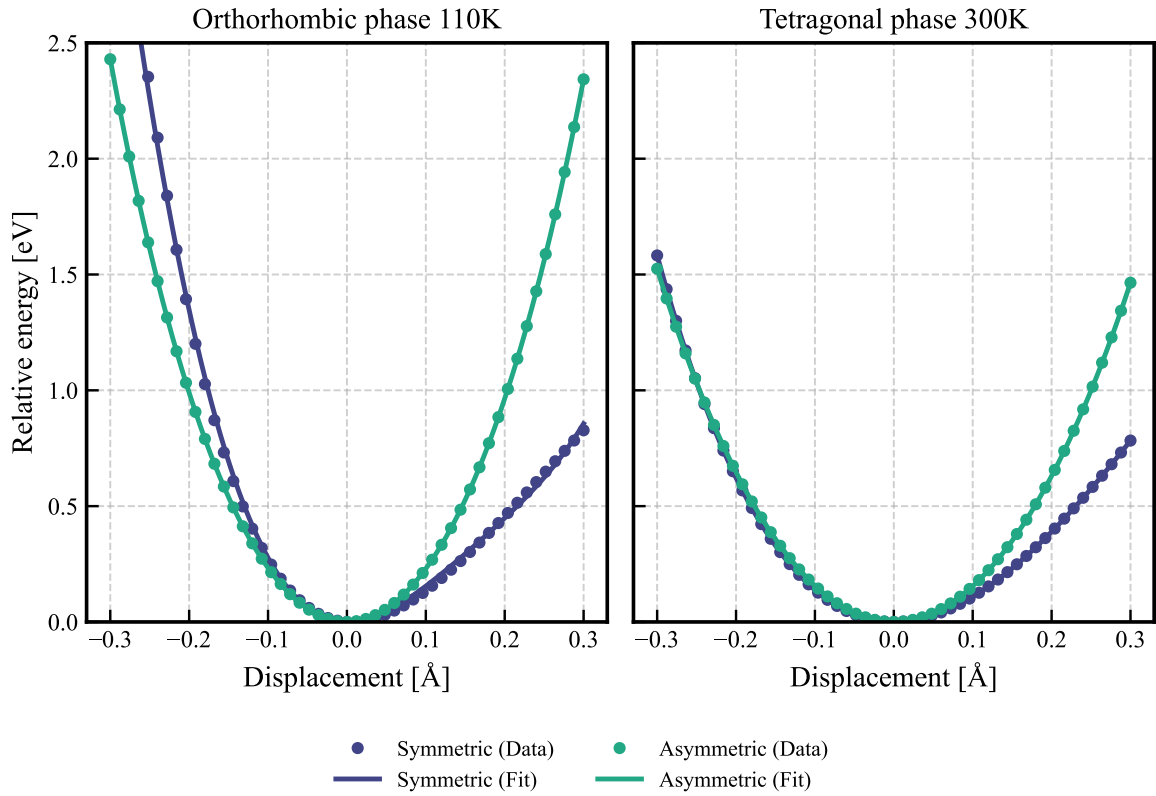


FIG. S13. Extended anharmonic potential fits for N–H stretching in MAPI. Left: Orthorhombic phase at 110K; Right: Tetragonal phase at 300K. Data points (symbols) and polynomial fits (lines) are plotted versus displacement (Å), with positive displacements indicating bond elongation.

S9. PATH-INTEGRAL SIMULATIONS OF HIGH-PRESSURE LIQUID WATER: RESOLVING SUBTLE VIBRATIONAL SHIFTS

As a case study, we examine liquid water under high-pressure conditions. Experimental Raman data indicate that increasing pressure from 0.05 GPa to 0.40 GPa strengthens hydrogen bonds, leading to a slight red shift (less than 15 cm^{-1}) in the O–H stretching frequency²⁷. This shift arises from the elongation and weakening of the intramolecular O–H bond due to enhanced intermolecular interactions. However, accurately capturing such subtle shifts poses a significant challenge for any computational method.

To investigate these effects, we analyze the vibrational density of states (VDOS) instead of directly computing Raman spectra. In order to accurately deconvolute overlapping features in our simulated VDOS spectra, we fitted the O–H vibrational bands using two skewed Lorentzian functions. Given that the separation between peaks is less than 5 cm^{-1} and that the individual Lorentzian components are substantially overlapped, a conventional unweighted fit is prone to inaccuracies and potential peak misassignments. To address this challenge, we implemented a dynamic weighting scheme that preferentially emphasizes data points in the peak regions while down-weighting the tails. This approach has been successfully applied to deconvolution of overlapping resonances in NMR spectroscopy²⁸ and determination of spectroscopic parameters from experimental IR absorption spectra^{29–32} and is now widely accepted as a standard data reduction methodology³³.

Our VDOS results (Figure S14) serve as a benchmark to assess the capability of different path integral molecular dynamics (PIMD) methods in resolving these small frequency shifts. To determine the maximum of the O–H stretching band, we identify the frequency corresponding to the highest intensity in spectra smoothed using a Blackmann window² with a 5 ps lag. Classical molecular dynamics (MD) simulations reproduce the expected trends: lower frequencies correspond to higher-pressure conditions. All PIMD methods exhibit a systematic red shift of approximately 85 cm^{-1} relative to classical vibrational frequencies, reflecting nuclear quantum effects (NQEs) even at ultra-high pressures and room temperature. Among the methods examined, thermostatted ring-polymer molecular dynamics (TRPMD) accurately reproduces the experimental trend despite suffering from spurious broadening, a known limitation of the method. Although small, the separation between vibrational peaks (approximately 4 cm^{-1}) is consistent between TRPMD and classical MD. Similarly, PA- T_e -CMD captures the correct experimental trend, with peak separations differing by less than 1 cm^{-1} relative to TRPMD, yielding better resolved spectra.

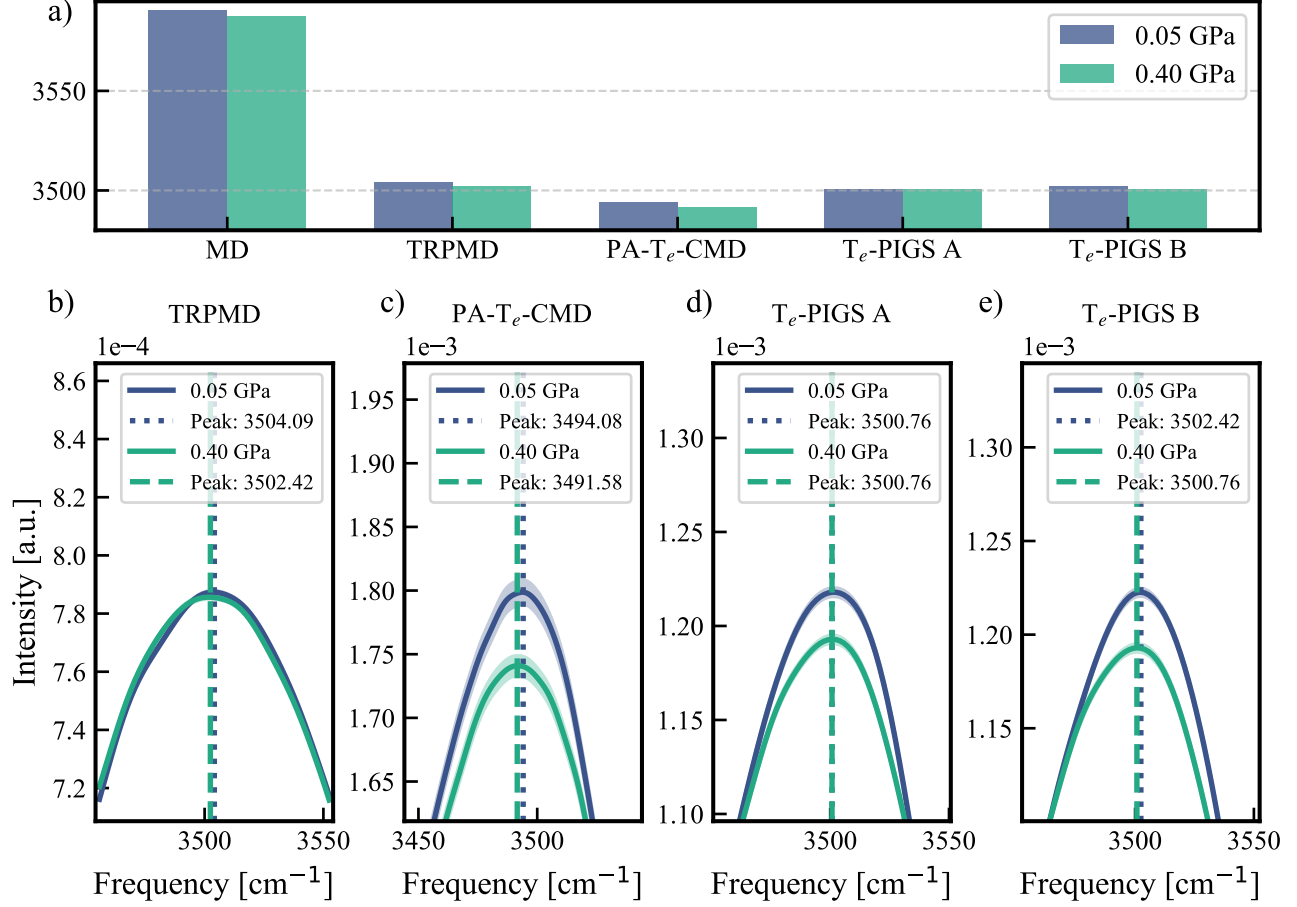


FIG. S14. Vibrational density of states (VDOS) of liquid water at different pressures, computed using classical MD, TRPMD, PA-T_e-CMD, and T_e-PIGS. The effects of nuclear quantum effects (NQE) and pressure-induced spectral shifts are analyzed. The comparison highlights differences in peak resolution and broadening among the methods.

Conversely, T_e-PIGS exhibits difficulties in resolving these subtle spectral shifts. This limitation stems from its reliance on a machine-learned potential of mean force (PMF), which may not fully capture pressure-dependent configurational changes. Specifically, when using a PMF trained only on the high-pressure system (denoted T_e-PIGS A), the method predicted nearly identical peak positions at both pressures, with differences within the spectral resolution. Only when a dedicated PMF is trained for each pressure condition (denoted T_e-PIGS B) does the method correctly resolve the pressure-dependent spectral trend, with peak separations comparable to PA-T_e-CMD.

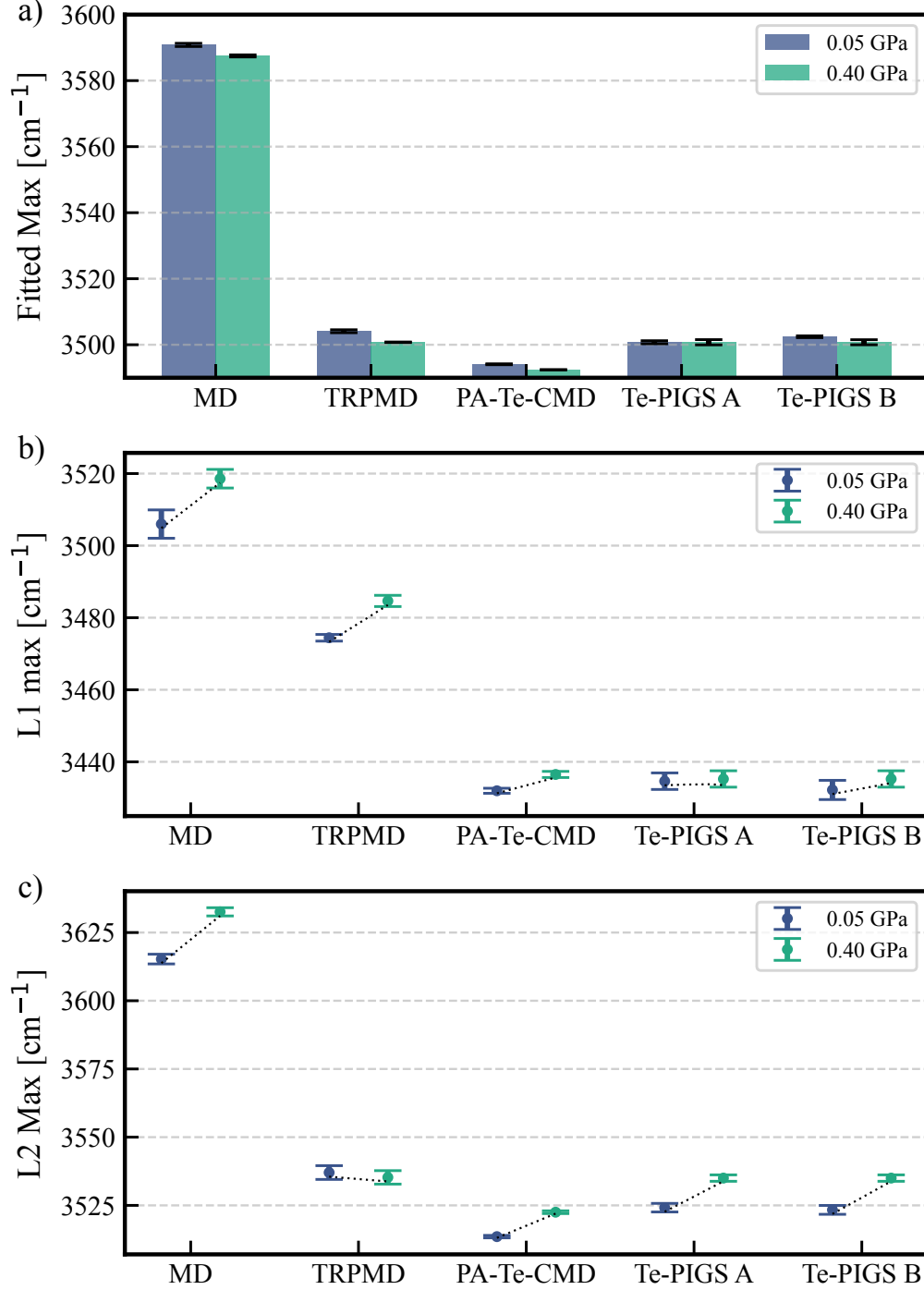


FIG. S15. (a) Bar chart comparing the fitted maximum frequencies obtained from a composite model for different simulation methods. (b) Error-bar plot of the first Lorentzian (L1) peak centers for the same methods and conditions. (c) Error-bar plot of the second Lorentzian (L2) peak centers.

To further support our VDOS-based peak assignments, we performed a dynamically weighted nonlinear least-squares fitting of the O-H vibrational bands using two skewed Lorentzian func-

tions to model water symmetric and asymmetric O–H stretching modes. The maxima of the fitted curves (Figure S15a) confirm the same trend observed in the raw data (Figure S14). Moreover, the individual Lorentzian components L1 and L2 (Figure S15b-c) show trends consistent with experimental high-pressure water studies²⁷, where both symmetric and asymmetric stretching frequencies shift to higher values with increasing pressure.

These findings further validate our VDOS-based analysis and reinforce the reliability of the bare peak assignments. More importantly, they highlight a fundamental limitation of T_e -PIGS: its ability to capture small vibrational shifts depends strongly on the similarity between the configurations sampled at the elevated temperature (used to compute the centroid PMF) and those relevant at the target system temperature. If the sampled ensembles differ significantly, a dedicated machine-learned PMF must be trained for each simulation condition to recover spectral trends accurately. In contrast, PA- T_e -CMD provides a more transferable approach, maintaining predictive accuracy across a broader range of conditions with a single parameter set, albeit at a higher computational cost.

S10. ADDITIONAL TABLES

S10.1. VDOS frequencies of CAF at 100K

MD [cm^{-1}]	TRPMD [cm^{-1}]	TRPMD-GLE [cm^{-1}]	PA- T_e -CMD [cm^{-1}]	T_e -PIGS [cm^{-1}]
379.89 (f1)	420.66 (d1)	452.16 (c1)	426.22 (b1)	400.28 (a1)
615.24 (f2)	594.86 (d2)	609.68 (c2)	598.56 (b2)	611.53 (a2)
685.66 (f3)	702.34 (d3)	700.48 (c3)	700.48 (b3)	693.07 (a3)
820.94 (f4)	813.53 (d4)	813.53 (c4)	815.38 (b4)	833.91 (a4)
930.27 (f5)	930.27 (d5)	943.25 (c5)	930.27 (b5)	980.31 (a5)
980.31 (f5)	1182.30 (d6)	1200.83 (c6)	1197.12 (b6)	1160.06 (a6)
1080.38 (f6)	1443.59 (d7)	1458.42 (c7)	1460.27 (b7)	1515.86 (a7)
1178.59 (f6)	1610.37 (d7)	1615.93 (c7)	1543.66 (b7)	1543.66 (a7)
1469.54 (f7)	1795.69 (d8)	1803.10 (c8)	1627.05 (b7)	1591.84 (a7)
1536.25 (f7)	–	–	1812.36 (b8)	1801.25 (a8)
1617.79 (f7)	–	–	–	2266.38(a9)
1830.90 (f8)	–	–	–	2698.16(a10)
2483.20 (f9)	–	–	–	–
2890.89 (f10)	–	–	–	–

TABLE S7. Detected CAF peak frequencies for different methods at 100 K.

S10.2. VDOS frequencies of MAPI at 300K

T_e -PIGS [cm^{-1}]	PA- T_e -CMD [cm^{-1}]	Experiment [cm^{-1}]	T_e -PIGS Difference [cm^{-1}]	PA- T_e -CMD Difference [cm^{-1}]
920.23 (a1)	920.33 (b1)	911.25	8.99	9.09
991.49 (a2)	993.11 (b2)	961.39	30.10	31.72
1256.16 (a3)	1251.37 (b3)	1249.71	6.45	1.66
1429.21 (a4)	1426.24 (b4)	1422.32	6.89	3.92
1478.07 (a5)	1476.78 (b5)	1469.57	8.50	7.21
1581.90 (a7)	1576.34 (b7)	1574.67	7.23	1.67

TABLE S8. Frequency differences between selected T_e -PIGS, PA- T_e -CMD vibrational frequencies, and the experimental IR bands at 300 K³⁴.

S10.3. VDOS frequencies of MAPI at 110K

T _e -PIGS [cm ⁻¹]	PA-T _e -CMD [cm ⁻¹]	Experiment [cm ⁻¹]	T _e -PIGS Difference [cm ⁻¹]	PA-T _e -CMD Difference [cm ⁻¹]
928.38 (d1)	927.91 (e1)	918.00	10.38	9.92
1005.74 (d2)	1011.81 (e2)	967.18	38.57	44.64
1270.41 (d3)	1267.54 (e3)	1252.60	17.81	14.94
1431.25 (d4)	1427.76 (e4)	1419.42	11.83	8.34
1457.71 (d5)	1456.56 (e5)	1451.24	6.47	5.32
1478.07 (d6)	1472.74 (e6)	1477.28	0.79	-4.54
1596.16 (d7)	1592.01 (e7)	1585.28	10.88	6.73
3009.08 (d8)	3017.24 (e8)	3024.95	-15.87	-7.71
3125.13 (d9)	3123.88 (e9)	3125.24	-0.11	-1.36

TABLE S9. Frequency differences between selected T_e-PIGS, PA-T_e-CMD vibrational frequencies, and the experimental IR bands at 110K³⁴.

S10.4. Fitting of liquid water VDOS spectra

Method	Fitted Max		Δ Max	L1 Peak		Δ L1	L2 Peak		Δ L2
	0.05 GPa	0.40 GPa		0.05 GPa	0.40 GPa		0.05 GPa	0.40 GPa	
MD	3590.82 \pm 0.48	3587.48 \pm 0.28	3.34	3505.98 \pm 3.93	3518.57 \pm 2.58	12.59	3615.28 \pm 1.78	3632.59 \pm 1.51	17.31
TRPMD	3504.09 \pm 0.44	3500.76 \pm 0.00	3.34	3474.43 \pm 0.92	3484.65 \pm 1.56	10.22	3537.03 \pm 2.52	3535.26 \pm 2.47	1.77
PA-Te-CMD	3494.08 \pm 0.14	3492.42 \pm 0.00	1.67	3431.96 \pm 0.70	3436.49 \pm 0.85	4.53	3513.55 \pm 0.45	3522.50 \pm 0.50	8.95
Te-PIGS A	3500.76 \pm 0.41	3500.76 \pm 0.80	0.00	3434.62 \pm 2.29	3435.24 \pm 2.27	0.62	3524.16 \pm 1.57	3535.00 \pm 1.17	10.85
Te-PIGS B	3502.42 \pm 0.24	3500.76 \pm 0.79	1.67	3432.19 \pm 2.67	3435.24 \pm 2.27	3.05	3523.35 \pm 1.63	3535.00 \pm 1.17	11.65

TABLE S10. Summary of Fitting Results. Uncertainties represent one standard deviation. All values are in cm⁻¹.

REFERENCES

- ¹G. Trenins and S. C. Althorpe, The Journal of Chemical Physics **149**, 014102 (2018).
- ²F. Harris, Proceedings of the IEEE **66**, 51 (1978).
- ³H. Partridge and D. W. Schwenke, The Journal of Chemical Physics **106**, 4618 (1997).
- ⁴F. Musil, I. Zaporozhets, F. Noé, C. Clementi, and V. Kapil, The Journal of Chemical Physics **157**, 181102 (2022).
- ⁵V. Kapil, D. P. Kovács, G. Csányi, and A. Michaelides, Faraday Discussions **249**, 50 (2024).
- ⁶I. Zaporozhets, F. Musil, V. Kapil, and C. Clementi, The Journal of Chemical Physics **161**, 134102 (2024).
- ⁷M. T. Weller, O. J. Weber, P. F. Henry, A. M. Di Pumpo, and T. C. Hansen, Chemical Communications **51**, 4180 (2015).
- ⁸I. Batatia, D. P. Kovacs, G. N. C. Simm, C. Ortner, and G. Csanyi, in *Advances in Neural Information Processing Systems*, edited by A. H. Oh, A. Agarwal, D. Belgrave, and K. Cho (2022).
- ⁹I. Batatia, S. Batzner, D. P. Kovács, A. Musaelian, G. N. C. Simm, R. Drautz, C. Ortner, B. Kozinsky, and G. Csányi, “The design space of e(3)-equivariant atom-centered interatomic potentials,” (2022), arXiv:2205.06643.
- ¹⁰J. Heyd, G. E. Scuseria, and M. Ernzerhof, The Journal of Chemical Physics **118**, 8207 (2003).
- ¹¹A. V. Krukau, O. A. Vydrov, A. F. Izmaylov, and G. E. Scuseria, The Journal of Chemical Physics **125**, 224106 (2006).
- ¹²A. Tkatchenko, R. A. DiStasio, R. Car, and M. Scheffler, Physical Review Letters **108**, 236402 (2012).
- ¹³A. D. Becke, The Journal of Chemical Physics **98**, 5648 (1993).
- ¹⁴P. J. Stephens, F. J. Devlin, C. F. Chabalowski, and M. J. Frisch, The Journal of Physical Chemistry **98**, 11623 (1994).
- ¹⁵A. Tkatchenko and M. Scheffler, Phys. Rev. Lett. **102**, 073005 (2009).
- ¹⁶L. Martínez, R. Andrade, E. Birgin, and J. M. Martínez, Journal of Computational Chemistry **30**, 2157 (2009).
- ¹⁷G. Bussi, T. Zykova-Timan, and M. Parrinello, The Journal of Chemical Physics **130**, 074101 (2009).
- ¹⁸S. Habershon, T. E. Markland, and D. E. Manolopoulos, The Journal of Chemical Physics **131**, 024501 (2009).

- ¹⁹Y. Litman, V. Kapil, Y. M. Y. Feldman, D. Tisi, T. Begušić, K. Fidanyan, G. Fraux, J. Higer, M. Kellner, T. E. Li, E. S. Pós, E. Stocco, G. Trenins, B. Hirshberg, M. Rossi, and M. Ceriotti, *The Journal of Chemical Physics* **161**, 062504 (2024).
- ²⁰G. Bussi, D. Donadio, and M. Parrinello, *The Journal of Chemical Physics* **126**, 014101 (2007).
- ²¹G. Bussi and M. Parrinello, *Computer Physics Communications* **179**, 26 (2008), special issue based on the Conference on Computational Physics 2007.
- ²²M. Rossi, V. Kapil, and M. Ceriotti, *The Journal of Chemical Physics* **148**, 102301 (2017).
- ²³M. Ceriotti, V. Kapil, P. Gasparotto, and D. Hollas, “Gle4md: Generalized langevin equation thermostat repository,” <http://gle4md.org/>, accessed: August 21, 2025.
- ²⁴Y. Rubner, C. Tomasi, and L. Guibas, in *Sixth International Conference on Computer Vision (IEEE Cat. No.98CH36271)* (1998) pp. 59–66.
- ²⁵N. Michaud-Agrawal, E. J. Denning, T. B. Woolf, and O. Beckstein, *Journal of Computational Chemistry* **32**, 2319 (2011).
- ²⁶Richard J. Gowers, Max Linke, Jonathan Barnoud, Tyler J. E. Reddy, Manuel N. Melo, Sean L. Seyler, Jan Domański, David L. Dotson, Sébastien Buchoux, Ian M. Kenney, and Oliver Beckstein, in *Proceedings of the 15th Python in Science Conference*, edited by Sebastian Benthall and Scott Rostrup (2016) pp. 98 – 105.
- ²⁷T. Okada, K. Komatsu, T. Kawamoto, T. Yamanaka, and H. Kagi, *Spectrochimica Acta Part A: Molecular and Biomolecular Spectroscopy* **61**, 2423 (2005), georaman 2004: Sixth International Conference on Raman Spectroscopy Applied to the Earth and Planetary Sciences.
- ²⁸G. T. Gipson, K. S. Tatsuoka, B. C. Sweatman, and S. C. Connor, *Journal of Magnetic Resonance* **183**, 269 (2006).
- ²⁹D. Benner, C. P. Rinsland, V. Devi, M. A. H. Smith, and D. Atkins, *Journal of Quantitative Spectroscopy and Radiative Transfer* **53**, 705 (1995).
- ³⁰D. M. Haaland, R. G. Easterling, and D. A. Vopicka, *Applied Spectroscopy* **39**, 73 (1985).
- ³¹J. Johns, *Journal of Molecular Spectroscopy* **125**, 442 (1987).
- ³²Y. S. Chang and J. H. Shaw, *Applied Spectroscopy* **31**, 213 (1977).
- ³³P. Bevington and D. Robinson, *Data Reduction and Error Analysis for the Physical Sciences* (McGraw-Hill Education, 2003).
- ³⁴G. Schuck, D. M. Többs, M. Koch-Müller, I. Efthimiopoulos, and S. Schorr, *The Journal of Physical Chemistry C* **122**, 5227 (2018).